Shadowing effects on J/ψ and Υ production at energies available at the CERN Large Hadron Collider

R. Vogt

Phys. Rev. C **92**, 034909 — Published 17 September 2015

DOI: 10.1103/PhysRevC.92.034909

Shadowing Effects on J/ψ and Υ Production at the LHC

R. Vogt
Lawrence Livermore National Laboratory,
Livermore, CA 94551, USA
and
Physics Department, University of California at Davis,
Davis, CA 95616, USA

Background: Proton-nucleus collisions have been used as a intermediate baseline for the determination of cold medium effects. They lie between proton-proton collisions in vacuum and nucleus-nucleus collisions which are expected to be dominated by hot matter effects. Modifications of the quark densities in nuclei relative to those of the proton are well established although those of the gluons in the nucleus are not well understood. The effect of these modifications on quarkonium production are studied in proton-lead collisions at the LHC at a center of mass energy of 5.02 TeV.
Purpose: The possibility of whether the LHC proton-lead data can be described by nuclear modifications of the parton densities, referred to as shadowing, alone is examined. The results are compard to the nuclear modification factor and to the forward-backward ratio, both as a function of transverse momentum, p_T, and rapidity, y.
Methods: The color evaporation model of quarkonium production is employed at next-to-leading order in the total cross section and leading order in the transverse momentum dependence. The EPS09 NLO modifications are used as a standard of comparison. The effect of the proton parton density and the choice of shadowing parameterization on the p_T and rapidity dependence of the result is studied. The consistency of the shadowing calculations at leading and next-to-leading order are checked.
The size of the mass and scale uncertainties relative to the uncertainty on the shadowing parameterization is also investigated. Finally, whether the expected cold matter effect in nucleus-nucleus collisions can be modeled as the product of proton-nucleus results at forward and backward rapidity is studied.
Results: The rapidity and p_T dependence of the nuclear modification factor is found to be generally consistent with the next-to-leading order calculations in the color evaporation model. The forward-backward ratio is more difficult to describe with shadowing alone. The leading and next-to-leading order calculations are inconsistent for EPS09 while other available parameterizations are consistent. The mass and scale uncertainties on quarkonium production are larger than those of the nuclear parton densities.
Conclusions: While shadowing is consistent with the nuclear suppression factors within the uncertainties, it is not consistent with the measured forward-backward asymmetry, especially as a function of transverse momentum. Data from $p + p$ collisions at the same energy are needed.

I. INTRODUCTION

This paper concentrates on comparison to the 2013 LHC p+Pb data on quarkonium production at $\sqrt{s_{NN}} = 5.02$ TeV. The inclusive J/ψ and Υ production data, binned as a function of rapidity and p_T (J/ψ) or rapidity alone (Υ), come from the ALICE [1–3] and LHCb [4, 5] collaborations. The detector acceptances for each experiment are briefly discussed in turn here. A more complete description of the data is provided in Sec. II.

Runs with mass asymmetric beams are different at the LHC than at RHIC because the LHC beams are not symmetric in energy. Instead, in the 2013 LHC p+Pb run a 4 TeV proton beam interacted with a $4(Z_{\rm Pb}/A_{\rm Pb}) = 1.58$ TeV/nucleon Pb beam. The nucleon-nucleon center of mass frame does not coincide with the laboratory frame in an energy-asymmetric collision system. Instead the center of mass frame is shifted by $\Delta y = 0.465$, taken to be in the direction of the proton beam, as defined by experiments. In addition, the ALICE and LHCb detector systems are not symmetric around the interaction point, with muon spectrometers on only one side of midrapidity. Therefore the beams have to be run in two modes, Pb+p and p+Pb. In the first case the lead beam is defined to move toward forward rapidity while in the second, the proton beam does. Because the second configuration is most similar to fixed-target operation and corresponds to small parton momentum fractions in the nucleus, both setups are analyzed according to the convention that the proton beam moves to positive rapidity. Thus the case of Pb+p collisions corresponds to larger parton momentum fractions in the nucleus.

The ALICE J/ψ measurement has been presented in both the central and forward/backward regions. Their muon spectrometer covers the pseudorapidity range $-4 < y_{\rm lab} < -2.5$ in the laboratory frame. Due to the rapidity shift in the asymmetric energy beams, the backward rapidity range for dimuon coverage is $-4.46 < y_{\rm cms} < -2.96$

while the forward rapidity range for dimuon coverage is $2.03 < y_{\rm cms} < 3.53$. The ALICE central detector includes dielectron coverage for $|y_{\rm lab} < 0.8|$. The quarkonium measurements in this region correspond to the rapidity range $-1.37 < y_{\rm cms} < 0.43$.

The LHCb detector covers $2 < y_{\rm lab} < 5$ in the laboratory frame. Like ALICE, they define the forward direction as the direction of the proton beam so that their backward coverage is $-5 < y_{\rm cms} < -2.5$ and the forward coverage is $1.5 < y_{\rm cms} < 4$.

Because there is not yet a measured $p + p$ baseline, the nuclear modification factor,

$$R_{p{\rm Pb}}(y, p_T) = \frac{d\sigma_{p{\rm Pb}}(y, p_T)/dydp_T}{T_{p{\rm Pb}}d\sigma_{pp}(y, p_T)/dydp_T} \ , \tag{1}$$

relies on an interpolation of the $p + p$ cross section. The rapidity shift was taken into account to obtain the $p + p$ cross section in the rapidity ranges of the p+Pb measurement. The factor $T_{p{\rm Pb}}$ in the denominator of Eq. (1) takes the centrality of the collision into account and is calculated in a Glauber model [1]. In this paper, only the minimum bias results are studied. See Ref. [6] for a discussion of the centrality dependence of the J/ψ measurement at RHIC. Work is in progress on the centrality dependence at the LHC [7].

In addition to studying the nuclear modification factors in these rapidity ranges, the forward-backward ratio,

$$R_{FB}(y, p_T) = \frac{d\sigma_{p{\rm Pb}}(y > 0, p_T)/dydp_T}{d\sigma_{p{\rm Pb}}(y < 0, p_T)/dydp_T} \ , \tag{2}$$

has also been presented [1, 4]. The unmeasured quantities $T_{p{\rm Pb}}$ and σ_{pp} cancel for a rapidity range symmetric around $y_{\rm cms} = 0$. Therefore R_{FB} is formed in the rapidity region where the forward and backward acceptances completely overlap, $2.96 < |y_{\rm cms}| < 3.53$ for ALICE and $2.5 < |y_{\rm cms}| < 4$ for LHCb. Some systematic uncertainties also cancel in the ratio. This ratio is perhaps a more faithful representation of cold matter effects on the p+Pb cross section. However, for theoretical interpretation, $R_{p{\rm Pb}}$ is still desirable because even a wrong model can produce the right ratio.

In a previous paper [8], predictions were made for pA collisions at $\sqrt{s_{_{NN}}} = 8.8$ and 5.5 TeV and ratios were formed both to $p + p$ collisions at the same energy and to $p + p$ collisions at the anticipated top energy of $\sqrt{s} = 14$ TeV. These calculations were made before the LHC turned on and so did not employ the same energies at which data were ultimately taken in LHC Run I: $\sqrt{s} = 2.76$, 7 and 8 TeV for $p+p$ collisions and 5.02 TeV for p+Pb. These calculations assumed that the leading and next-to-leading order treatments of the modifications of the parton densities in nuclei, when employed consistently, would be identical, as discussed in more detail later.

More recently, calculations were made for the nuclear modification factor as a function of y and p_T at the energy appropriate for the p+Pb run [9] but not taking the rapidity shift into account for the p_T acceptance. In addition, the p_T dependent ratio was presented for forward rapidity only. These predictions, along with other, updated, CEM calculations with EPS09 NLO nuclear parton densities (nPDFs) were compared to the ALICE and LHCb J/ψ and Υ data [1–5, 10–12]. In those calculations, the incorrect factorization scale, μ_F, was passed to the nuclear parton densities. (The square of the scale was passed instead of the scale itself, as required by most shadowing parameterizations, so that the overall cold matter effect was reduced relative to the true value. This was not the case for the LO predictions in Ref. [8].) In this paper, this error is corrected and the p_T-dependent ratios calculated in the CEM are presented for the first time.

In the next section, Sec. II, a brief summary of the ALICE and LHCb J/ψ and Υ measurements is provided to place the calculations in context.

The calculation of quarkonium production in $p+p$ collisions is summarized in Sec. III. The J/ψ and Υ distributions obtained with several different sets of proton parton densities are compared. Comparison of these calculations to available $p+p$ data can be found in Refs. [13, 14]. A short summary of cold nuclear matter effects is given in Sec. IV.

The nuclear parton density modifications used in this paper are described in Sec. V. The calculations are compared to the p+Pb data from ALICE and LHCb on J/ψ and Υ production at $\sqrt{s_{_{NN}}} = 5$ TeV in Sec. VI. Both $R_{p{\rm Pb}}$ and R_{FB} are calculated as functions of rapidity and transverse momentum. The data are first compared to the EPS09 uncertainty bands. The leading order (LO) and next-to-leading order (NLO) results are contrasted for order-by-order consistency. Next, the data are compared to all the nuclear parton densities discussed in Sec. V to see if any parameterizations are particularly favored. The mass and scale dependence of the results is also shown. Finally, how closely the $A+A$ calculations can be reproduced by a convolution of $p+A$ and $A+p$ collisions is tested. A comparison to the RHIC data is also made.

II. DESCRIPTION OF THE p+PB QUARKONIUM DATA

In this section, the quarkonium data for J/ψ and $\Upsilon(1S)$ from ALICE and LHCb are described. Since there has been no $p+p$ run at $\sqrt{s} = 5$ TeV to date, the denominator of $R_{p{\rm Pb}}$ has to be interpolated between available measurements at other energies. The $p+p$ cross sections also had to be adjusted to the rapidity ranges of the p+Pb measurement.

The interpolation methods used by the collaborations depend on the quarkonium state, the observable, and the previously available data. However, in all cases, the quarkonium states were assumed to be produced unpolarized.

To obtain $R_{p\mathrm{Pb}}(y)$ for the J/ψ, the ALICE Collaboration used an energy interpolation between their $p+p$ measurements at 2.76 and 7 TeV to obtain the $\sqrt{s}$ dependence of the $p+p$ cross section. They presented their J/ψ p+Pb data in both a single rapidity interval as well as in six rapidity bins measured for $p+p$ collisions (of course without the rapidity shift in $p+p$). These first results were for $R_{p\mathrm{Pb}}$ at forward and backward rapidity and R_{FB} as a function of p_T and y [1].

Their energy interpolation was based on three assumed shapes: linear, power law and exponential. The central value of the result for each rapidity bin is an average of the three shapes while the uncertainty is the quadrature sum of a term related to the uncertainty on the data used for the interpolation and a term related to the spread between results with different shapes.

An additional small systematic uncertainty was obtained by comparing the shapes with those of the leading order CEM and the fixed-order next-to-leading logarithm (FONLL) approach for inclusive open heavy flavor production [1]. Note that the LO and NLO CEM energy dependence should be similar if the same mass and scale parameters, as well as the same proton parton densities are used. (The shapes will not be similar if *e.g.* CTEQ6M is used at NLO and CTEQ61L is used at LO.) Using the FONLL calculation for the total $c\overline{c}$ cross section may produce a shape similar to the CEM but the magnitude, of course, will be quite different.

In a later paper, the ALICE Collaboration presented results for the midrapidity $R_{p\mathrm{Pb}}$, a bin around $-1.37 < y_{\mathrm{cms}} < -0.43$ to add to $R_{p\mathrm{Pb}}(y)$ as well as the ratios $R_{p\mathrm{Pb}}(p_T)$ at forward, backward and midrapidity [2]. While the forward-backward ratio as a function of p_T was published in Ref. [1], the separate values of $R_{p\mathrm{Pb}}(p_T)$ were not yet available.

The $p+p$ baseline for the p_T-dependent ratios was obtained through interpolation. At midrapidity, data from $\sqrt{s} = 0.2$, 1.96, 2.76 and 7 TeV were used. The 1.96 TeV results from $p\overline{p}$ collisions from the Tevatron were considered on the same basis as $p+p$ collisions because, at these high energies, production is dominated by the gg process. Scaling in $x_T = m_T/\sqrt{s}$ was used to compare the disparate energies. Only exponential, logarithmic and power law dependencies were considered in this case because there is no p_T dependence in the LO CEM and the FONLL approach is for single inclusive distributions, not pairs, so the p_T slope is not available from these calculations.

At forward rapidity, the only data available to include in the $\sqrt{s}$ interpolation are the 2.76 and 7 TeV data from ALICE. (They did not employ the LHCb results in their interpolation.) In this region, the dependencies were linear, power law and exponential. The results for $R_{p\mathrm{Pb}}(p_T)$ are only shown up to 8 GeV because the $p+p$ data were limited to this p_T range. The non-prompt J/ψ production from b decays increases with p_T, giving a $\sim 20\%$ correction at $p_T \sim 8$ GeV [2].

ALICE has also measured the ψ' in p+Pb collisions, finding significantly more suppression [15]. Since this difference cannot be due to initial state effects alone, we do not address that result in this work.

The ALICE Collaboration also measured the inclusive Υ(1S) and Υ(2S) rates. The rapidity dependence of $R_{p\mathrm{Pb}}$ was reported in Ref. [3]. The Υ yields are not large so that only one rapidity bin is reported. To obtain the $p+p$ baseline for $R_{p\mathrm{Pb}}$, they used the LHCb results for Υ production at $\sqrt{s} = 2.76$, 7 and 8 TeV, divided into rapidity bins. They employed 21 different shapes, 15 from the LO CEM with different proton PDFs and factorization scale choices; 3 based on the FONLL b quark distributions; while linear, power-law, and exponential shapes rounded out the set. The agreement of all the shapes with the data was generally poor so the fits with the worst χ^2/dof were discarded for the final fits. In addition to the J/ψ uncertainties described above, they also considered small rapidity shifts between the ALICE and LHCb rapidity bins.

They found that the Υ $R_{p\mathrm{Pb}}$ is quite similar to that of J/ψ at forward rapidity while at negative rapidity the Υ $R_{p\mathrm{Pb}}$ is compatible with unity but lower than that of the J/ψ. This is a fairly remarkable result since nuclear effects are generally expected to be smaller for the Υ than for J/ψ so that the Υ $R_{p\mathrm{Pb}}$ should be closer to unity at low p_T where the difference in mass is the dominant effect. At higher p_T, where $p_T \gg m$, the results should be similar for the two quarkonium states.

They reported the Υ(2S)/Υ(1S) ratios at forward and backward rapidity, $0.26 \pm 0.09 \pm 0.04$ and $0.27 \pm 0.08 \pm 0.04$ respectively [3]. The result is consistent with the $p+p$ ratio at 7 TeV. This is also consistent with shadowing being the dominant cold matter effect since it affects the excited states the same way as the ground state.

The LHCb Collaboration has also measured J/ψ [4] and Υ [5] production in their muon spectrometer. In addition to the inclusive J/ψ result, they also separate $b \to J/\psi$ decays to present a non-prompt J/ψ result. Their primary functional dependence to interpolate between their p+p results at 2.76, 7 and 8 TeV is a power law, $\sigma(\sqrt{s}) = (\sqrt{s}/p_0)^{p_1}$.

---

[0] Note that the FONLL approach calculates the single inclusive heavy flavor distributions, not those of the $Q\overline{Q}$ pair as in the CEM.

Experiment	y acceptance	$N_{J/\psi}$ [Ref.]	$N_{\Upsilon(1S)}$ [Ref.]	$N_{\Upsilon(2S)}$ [Ref.]	$N_{\Upsilon(3S)}$ [Ref]
ALICE	$2.03 < y_{\rm cms} < 3.53$	$(6.69 \pm 0.05) \times 10^4$ [1]	305 ± 34 [3]	83 ± 23 [3]	-
	$-4.46 < y_{\rm cms} < -2.96$	$(5.67 \pm 0.05) \times 10^4$ [1]	161 ± 21 [3]	42 ± 14 [3]	-
	$-1.37 < y_{\rm cms} < -0.43$	465 ± 37 [2]	-	-	-
LHCb	$2.5 < y_{\rm cms} < 4.0$	25280 ± 240 [4]	189 ± 16 [5]	41 ± 9 [5]	13 ± 7 [5]
	$-4.0 < y_{\rm cms} < -2.5$	8830 ± 160 [4]	72 ± 14 [5]	17 ± 10 [5]	4 ± 8 [5]

TABLE I: The J/ψ and Υ yields from the ALICE and LHCb collaborations in their stated rapidity acceptance. The results are integrated over all p_T.

They use linear and exponential dependencies to obtain a systematic uncertainty on their interpolation. They do not use any production models for the energy interpolation [4]. A similar, power-law-based method is used to obtain the $p+p$ baseline for Υ production [5].

Recently, the ATLAS Collaboration has presented results on the forward-backward J/ψ ratio as a function of y in the region $8 < p_T < 30$ GeV and as a function of rapidity in the rapidity range $|y_{\rm cms}| < 1.94$ [16]. Their results for R_{FB} are consistent with unity within the uncertainties of the data. CMS also recently presented the prompt J/ψ R_{FB} as a function of p_T and as a function of rapidity for high p_T [17]. Their results are consistent with those of ATLAS.

The LHCb Υ measurement includes low statistics for the Υ(3S) states, as well as the 1S and 2S states. The ratios Υ(2S)/Υ(1S) are $0.28 \pm 0.14 \pm 0.05$ in the backward direction and $0.20 \pm 0.05 \pm 0.01$ at forward rapidity, both consistent with $p+p$ measurements [5]. While the Υ(3S)/Υ(1S) ratios are also consistent with those in $p+p$ collisions, their low statistics reduces their significance.

Finally, note that the intriguing CMS $\Upsilon(n\mathrm{S})/\Upsilon(1\mathrm{S})$ ratios measured as a function of both the number of tracks at midrapidity and the transverse energy at forward rapidity [18] are not addressed. This effect, also seen in $p+p$ collisions, is not attributable to initial-state modifications of the parton densities and, as such, is outside the scope of this work.

The quarkonium yields for all the ALICE and LHCb results discussed here are given in Table I.

III. PRODUCTION IN $p+p$ COLLISIONS

Following previous work [8, 13], quarkonium production is treated within the color evaporation model (CEM). In the CEM, heavy flavor and quarkonium production are treated on an equal footing. The CEM has enjoyed considerable phenomenological success when applied at NLO in the total cross section and LO in the quarkonium p_T distribution [13, 19–21]. (See Ref. [13] for comparison of the $\sqrt{s} = 2.76$ and 7 TeV ALICE data with the same CEM calculation employed here.)

A. Color Evaporation Model Calculation

In the CEM, the quarkonium production cross section is some fraction, F_C, of all $Q\overline{Q}$ pairs below the $H\overline{H}$ threshold where H is the lowest mass heavy-flavor hadron. Thus the CEM cross section is simply the $Q\overline{Q}$ production cross section with a cut on the pair mass but without any constraints on the color or spin of the final state. The color of the octet $Q\overline{Q}$ state is 'evaporated' through an unspecified process which does not change the momentum. The additional energy needed to produce heavy-flavored hadrons when the partonic center-of-mass energy, $\sqrt{\hat{s}}$, is less than $2m_H$, the $H\overline{H}$ threshold energy, is nonperturbatively obtained from the color field in the interaction region. Thus the quarkonium yield may be only a small fraction of the total $Q\overline{Q}$ cross section below $2m_H$. At leading order, the production cross section of quarkonium state C in a $p+p$ collision is

$$\sigma_C^{\rm CEM}(s_{_{NN}}) = F_C \sum_{i,j} \int_{4m^2}^{4m_H^2} d\hat{s} \int dx_1\, dx_2\; f_i^p(x_1, \mu_F^2)\; f_j^p(x_2, \mu_F^2)\; \mathcal{J}(\hat{s}) \hat{\sigma}_{ij}(\hat{s}, \mu_F^2, \mu_R^2) \ , \tag{3}$$

where $ij = q\overline{q}$ or gg and $\hat{\sigma}_{ij}(\hat{s})$ is the $ij \to Q\overline{Q}$ subprocess cross section. Here $\mathcal{J}(\hat{s})$ is a kinematics-dependent Jacobian. At LO $\mathcal{J}(\hat{s}) = \delta(\hat{s} - x_1 x_2 s)/s$, at NLO and for differential cross sections, the expressions are more complex.

The fraction F_C must be universal so that, once it is fixed by data, the quarkonium production ratios should be constant as a function of $\sqrt{s}$, y and p_T. The actual value of F_C depends on the heavy quark mass, m, the scale parameters, the parton densities and the order of the calculation.

The parameter $F_{J/\psi}$ is fit to both the full data set as well as to more limited sets. The final J/ψ result is based on the total cross section data with only p, Be, Li, C, and Si targets respectively. In this way, uncertainties due to ignoring any cold nuclear matter effects, which are on the order of a few percent in light targets, are avoided. The fits are restricted to the forward cross sections only, rather than including the $B_{ll}d\sigma/dy|_{y=0}$ data in the fits. The rapidity distributions calculated in the MNR code are subject to fluctuations about the mean, even with high statistics calculations. The total cross sections, not subject to these fluctuations, are thus more accurate. See Ref. [13] for more detail.

In the case of Υ production, however, most of the reported cross section values are for $B_{ll}d\sigma/dy|_{y=0}$. The branching ratio B_{ll} here is a composite for the three Υ S states which were not separated at fixed-target energies. For later experiments, with sufficient resolution to separate the mass peaks, the individual $y = 0$ cross sections were multiplied by the PDG values of the branching ratios and summed [14]. The data in the Υ fits are from fixed-target energies, $19.4 \leq \sqrt{s} \leq 44$ GeV, and collider data from the ISR, S$p\overline{p}$S and the Tevatron. The $p + \overline{p}$ data from the S$p\overline{p}$S and the Tevatron are fit with the same coefficient as the lower energy $p + p$ data. At $\sqrt{s} = 630$ GeV, the difference between the $p + p$ and $p + \overline{p}$ $b\overline{b}$ cross sections is less than 0.5%, too small to affect the fit results.

The same values of the charm quark mass and scale parameters as found in Ref. [13] are employed to obtain the normalization F_C for the J/ψ, $(m, \mu_F/m, \mu_R/m) = (1.27 \pm 0.09\,\text{GeV}, 2.1^{+2.55}_{-0.85}, 1.6^{+0.11}_{-0.12})$. In the case of Υ production, $(m, \mu_F/m, \mu_R/m) = (4.65 \pm 0.09\,\text{GeV}, 1.4^{+0.77}_{-0.49}, 1.1^{+0.22}_{-0.20})$ is used. The value of F_C is determined only for the central parameter set in each case and scale all the other calculations by the same value of F_C to obtain the extent of the J/ψ and Υ mass and scale uncertainty bands, as described in detail in Sec. VI E.

The value $F_{J/\psi} = 0.020393$ is found for the central result with $(m, \mu_F/m, \mu_R/m) = (1.27\,\text{GeV}, 2.1, 1.6)$ employing the CT10 parton densities [13]. The central $y = 0$ result, $F_{\Sigma\Upsilon} = 0.0077$, is obtained for the combined Υ S states with the CT10 parton densities and $(m, \mu_F/m, \mu_R/m) = (4.65\,\text{GeV}, 1.4, 1.1)$. After separating the S states, the inclusive $1S$ value is $F_\Upsilon = 0.022$ [14].

The CEM calculations use the NLO $Q\overline{Q}$ code of Mangano *et al.* (MNR) [22] with the $H\overline{H}$ mass cut in Eq. (3), as described in Refs. [19, 23]. Because the NLO $Q\overline{Q}$ code is an exclusive calculation, the mass cut is made on the invariant average over kinematic variables of the c and $\overline{c}$. Thus, instead of defining μ_F and μ_R relative to the quark mass, they are defined relative to the transverse mass, $\mu_{F,R} \propto m_T = \sqrt{m^2 + p_T^2}$ where p_T is that of the $Q\overline{Q}$ pair, $p_T^2 = 0.5(p_{T_Q}^2 + p_{T_{\overline{Q}}}^2)$.

At LO in the total cross section, the $Q\overline{Q}$ pair p_T is zero. Thus, while the calculation is NLO in the total cross section, it is LO in the quarkonium p_T distributions. In the exclusive NLO calculation [22] both the Q and $\overline{Q}$ variables are integrated to obtain the pair distributions, recall $\mu_{F,R} \propto m_T$.

Results on open heavy flavors indicate that some level of transverse momentum broadening is needed to obtain agreement with the low p_T data. This is often done by including some intrinsic transverse momentum, k_T, smearing to the initial-state parton densities. The implementation of intrinsic k_T in the MNR code is not handled in the same way as calculations of other hard processes due to the nature of the code. In the MNR code, the cancellation of divergences is done numerically. Since adding additional numerical Monte-Carlo integrations would slow the simulation of events, in addition to requiring multiple runs with the same setup but different intrinsic k_T kicks, the kick is added in the final, rather than the initial, state. In Eq. (3), the Gaussian function $g_p(k_T)$,

$$g_p(k_T) = \frac{1}{\pi\langle k_T^2\rangle_p} \exp(-k_T^2/\langle k_T^2\rangle_p) \ , \tag{4}$$

[24], multiplies the parton distribution functions for both hadrons, assuming the x and k_T dependencies in the initial partons completely factorize. If factorization applies, it does not matter whether the k_T dependence appears in the initial or final state if the kick is not too large. In Ref. [24], $\langle k_T^2\rangle_p = 1$ GeV^2, along with the Peterson fragmentation function with parameter $\epsilon = 0.06$, was found to best describe fixed-target charm production. Note that currently Peterson fragmentation with $\epsilon = 0.06$ is considered too strong. The FONLL fragmentation scheme for open heavy flavor is softer [25].

In the code, the $Q\overline{Q}$ system is boosted to rest from its longitudinal center-of-mass frame. Intrinsic transverse momenta of the incoming partons, $\vec{k}_{T1}$ and $\vec{k}_{T2}$, are chosen at random with k_{T1}^2 and k_{T2}^2 distributed according to Eq. (4). A second transverse boost out of the pair rest frame changes the initial transverse momentum of the $Q\overline{Q}$ pair, $\vec{p}_T$, to $\vec{p}_T + \vec{k}_{T1} + \vec{k}_{T2}$. The initial k_T of the partons could have alternatively been given to the entire final-state system, as is essentially done if applied in the initial state, instead of to the $Q\overline{Q}$ pair. There is no difference if the calculation is LO but at NLO an additional light parton can also appear in the final state so the correspondence is not exact. In Ref. [24], the difference between the two implementations is claimed to be small if $k_T^2 \leq 2$ GeV^2. The rapidity distribution, integrated over all p_T, is unaffected by the intrinsic k_T.

The effect of the intrinsic k_T on the shape of the quarkonium p_T distribution can be expected to decrease as $\sqrt{s}$ increases because the average p_T also increases with energy. However, the value of $\langle k_T^2 \rangle$ may increase with $\sqrt{s}$ so that effect remains important at higher energies. The form $\langle k_T^2 \rangle = 1 + (1/n)\ln(\sqrt{s}/20)$ GeV^2 is assumed. Using the RHIC J/ψ data, $n = 12$ gave the best description of the p_T distribution both at central and forward rapidity [13]. A larger value of n and thus of $\langle k_T^2 \rangle$ is required for the Υ p_T distribution. For Υ, $n = 3$ is set by comparison to the Tevatron results at $\sqrt{s} = 1.8$ TeV [14]. For this study, n is not modified by the nuclear medium.

Note that most approaches to quarkonium production: the CEM; the color singlet model (CSM); and the Nonrelativistic QCD approach (NRQCD), assume the validity of collinear factorization which separates the initial, nonperturbative parton densities from the perturbatively-calculable hard scattering that produces the final state. Collinear factorization is assumed to hold for quarkonium production in the CEM. Factorization has been proved for quarkonium production in NRQCD at high p_T [26] but not at low p_T. The open charm flavor results at low p_T at the LHC [13] agree with calculations employing collinear factorization [13] better than calculations employing k_T factorization [27]. Collinear factorization should work better for bottom since the factorization scale and the x region probed are both larger.

Since the start up of the LHC, several groups have performed global analyses of the nonperturbative matrix elements in the NRQCD approach up to NLO, see Ref. [28] and references therein for discussion and comparison of the results for J/ψ production data in $e^+ + e^-$, $e + p$, $p + p$ and $p + \overline{p}$ collisions. In Ref. [28], it is clear that the nonperturbative matrix elements are quite sensitive to the minimum p_T employed in the fits. These matrix elements do not appear to be universal since choosing different data sets to fit to result in quite different values of the matrix elements. Indeed, the agreement with the $e^+ + e^-$ and $e + p$ data is poor unless the minimum p_T is low, $p_T \sim 3$ GeV, but these fits cannot reproduce the measured high p_T quarkonium polarization [28].

In addition, if the fitted matrix elements are used to calculate the J/ψ cross section at $y = 0$ in $p + p$ collisions as a function of $\sqrt{s}$, good agreement with neither the shape nor the magnitude of the cross section can be obtained, see Ref. [29]. The results overshoot the measured cross sections significantly, sometimes by an order of magnitude [29]. This is not a surprising outcome because the the integrated $y = 0$ cross section is dominated by low p_T J/ψ production. In the same paper, the CSM cross sections are also compared to these data. It was found that only the LO CSM calculation produces a physical $\sqrt{s}$ dependence that agrees relatively well with the data, at NLO some values of μ_F give an unphysical energy dependence [29]. They also point out that the CEM produces the best agreement with the $\sqrt{s}$ dependence over the entire range.

Note that, while the CSM and NRQCD make predictions for the p_T dependence at relatively high p_T, the region of interest for nuclear effects on the parton densities, as addressed here, is at low p_T and the CEM, through the application of k_T smearing, is the only production model that addresses the entire p_T range. Since the average k_T is an energy-dependent parameter, ideally this should be replaced by a low-p_T resummation.

Some recent results may provide improvements for NRQCD, at least at collider energies [26, 30, 31]. References [30, 31] perform small x resummation in the color-glass condensate (CGC) in the NLO NRQCD approach with the nonperturbative matrix elements taken from the high p_T fits of Chao *et al.* [32]. The CGC gluon distribution is employed in the CGC+NRQCD calculation at low p_T. This matches well with the high p_T NLO NRQCD calculation in the intermediate p_T range. Thus the entire p_T range of the data can be described within the combined approaches, both in $p + p$ and $p + A$ collisions for forward rapidities and sufficiently high $\sqrt{s}$ [30, 31]. The energy dependence of $d\sigma/dy|_{y=0}$ is also reproduced quite well for $\sqrt{s} > 0.2$ TeV athough agreement with the midrapidity RHIC data is rather poor [30]. This approach is inapplicable at lower $\sqrt{s}$. Reference [26] presents a factorized power expansion for quarkonium production, including next-to-leading power (NLP) contributions to the perturbative part. This formalism requires fragmentation functions for heavy $Q\overline{Q}$ pairs as well as for light partons. With the fragmentation functions and the NLP contributions included in NRQCD, it was found that the ${}^3S_1^{[1]}$ and ${}^1S_0^{[8]}$ components of the cross section are dominated by the NLP contributions over all p_T, independent of the nonperturbative matrix elements [26]. This formalism describes J/ψ production well at collider energies for $p_T > 10$ GeV. The possible dominance of the ${}^1S_0^{[8]}$ contribution in the total production rate could explain the apparent unpolarized J/ψ production. This conclusion is consistent with the data-driven approach to polarization in Ref. [33].

The polarization has not yet been calculated in the CEM. While it should be straightforward at LO, to go to NLO one would have to start from a polarized $Q\overline{Q}$ pair production code.

B. Comparison of $p + p$ Results

The J/ψ and Υ p_T and rapidity distribution in $p + p$ collisions employing different proton parton densities are compared. The main results are obtained with the CT10 [34] parton densities, also used in the recent evaluations of

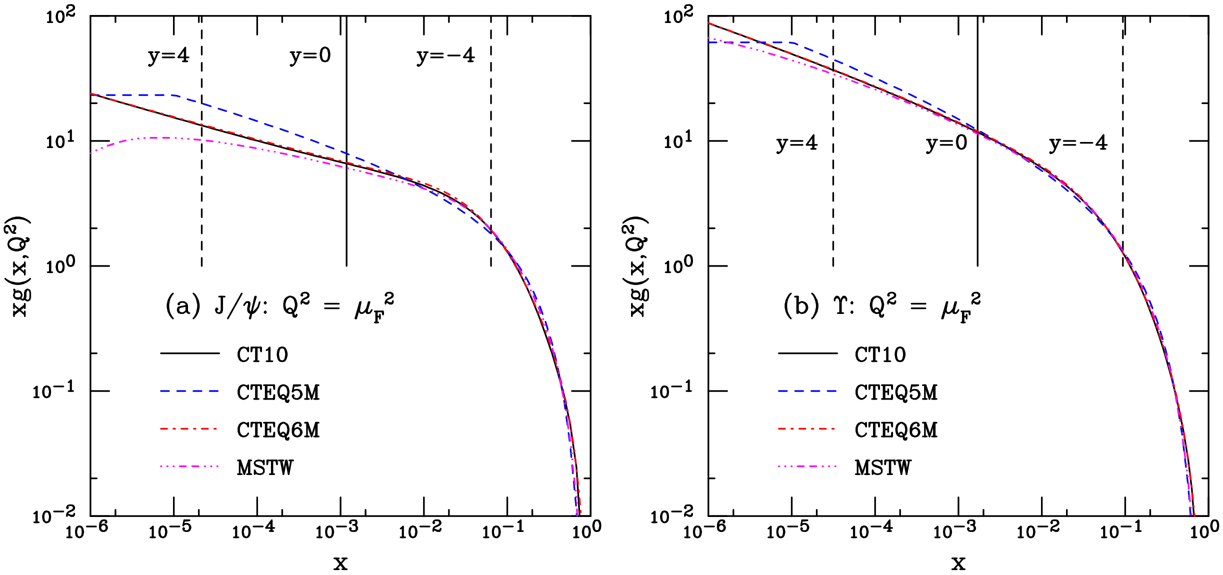

FIG. 1: (Color online) The gluon distribution function at the factorization scale for J/ψ (a) and Υ (b) production. The CT10 (black solid), CTEQ5M (blue dashed), CTEQ6M (red dot-dashed) and MSTW (magenta dot-dot-dot-dash-dashed) are compared, all calculated with the same input parameters.

the charm and bottom cross sections [13, 14] where good agreement with the present quarkonium data is found within the mass and scale uncertainties. In Fig. 1, the NLO CT10 gluon distributions are compared to those from CTEQ5M [35], CTEQ6M [36] and MSTW [37]. The MSTW central NLO set is a rather recent, frequently used parton density shown as an alternative to CT10. It is available at LO, NLO and NNLO and has a low starting scale of $\mu_0^2 = 1$ GeV^2. The CTEQ sets and CT10, at LO and NLO, have a starting scale of $\mu_0^2 = X$ GeV^2. The vertical lines at the top of the plots indicate the gluon density at forward, mid- and backward rapidity.

The CTEQ6M and CTEQ5M distributions were chosen because they have been used to extract the modifications of the parton densities in the nucleus. The CTEQ6M distributions were used in a global analysis of the nuclear modifications of the parton densities to obtain the EPS09 NLO sets [38]. They were also used in previous estimates of the quarkonium cross sections at the LHC [39]. The corresponding EPS09 LO sets were obtained based on the CTEQ61L densities, as discussed in more detail later. The CTEQ5M distributions were used to extract the NLO nuclear modifications in the FGS sets [40]. Older distributions used to extract nuclear modifications are CTEQ4L [41] and GRV LO [42] (EKS98 [43, 44]) and GRV98 LO and NLO [45] (nDS [46]). Since these proton PDFs are now outdated, they are not shown here.

Figure 1 shows the gluon densities in the proton at the scales used to calculate J/ψ (a) and Υ (b) production. The CT10 distributions, the most recent of all those considered, follow the previous CTEQ6 global analysis. The CT10 and CTEQ6M gluon distributions are almost identical. The earlier CTEQ5M set is quite different: the lowest x value included in the analysis is 10^{-5} and, instead of extrapolating smoothly to lower values of x, the density is frozen such that $xg(x < 10^{-5}, \mu^2) \equiv xg(x = 10^{-5}, \mu^2)$. It also tends to be higher than the other gluon PDFs for $10^{-5} < x < 10^{-2}$. The MSTW distribution is below the others for the J/ψ factorization scale. All the gluon distributions are more similar at the Υ scale even though CTEQ5M is still somewhat higher for $10^{-5} < x < 10^{-2}$.

The CTEQ6M and CT10 gluon distributions are zero at the minimum scale, $xg(x, \mu_0^2) = 0$. Thus they undergo rapid evolution at low x since they are based on a valence-like initial distribution, $x^\alpha (1-x)^\beta$. On the other hand, the MSTW sets allow a negative gluon density at low x. Therefore the MSTW gluon density exhibits a slower scale evolution. It will thus produce the smallest cross sections for J/ψ and Υ production while CTEQ5M will give the largest.

In Fig. 2, the shapes of the J/ψ p_T and y distributions are shown for the proton parton densities presented in Fig. 1. The p_T distributions are shown in the region of rapidity overlap with the shifted p+Pb range at forward rapidity, $2.96 < y < 3.53$. In $p+p$ collisions, the p_T distributions at forward and backward rapidity are identical because the y distributions are symmetric.

The results are given with the same CEM normalization, F_C, as found for the CT10 fits in Ref. [13]. Because the low x gluon distributions differ in shape and magnitude, the values of the cross sections also differ by as much as $15-20\%$. If fits of F_C were made with the three additional proton parton densities, the values of F_C would clearly

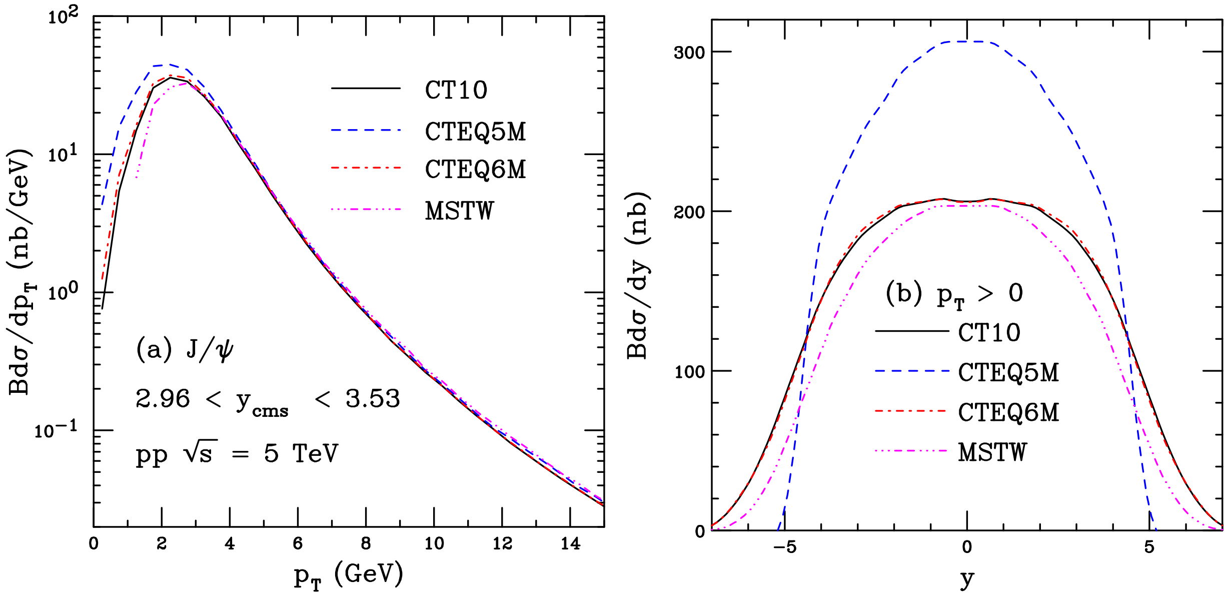

FIG. 2: (Color online) The J/ψ p_T distribution at forward rapidity in $p + p$ collisions (a) and the p_T-integrated y distribution (b). Results from CT10 (black solid), CTEQ5M (blue dashed), CTEQ6M (red dot-dashed) and MSTW (magenta dot-dot-dot-dash-dashed) are compared, all calculated with the same input parameters and using the same value of F_C as for CT10.

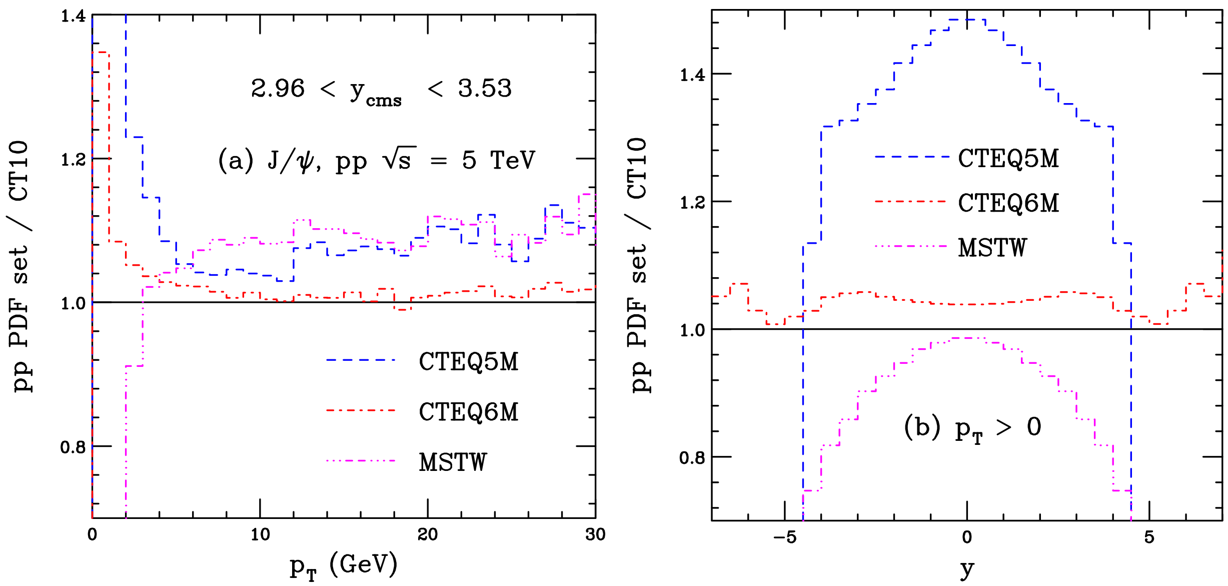

FIG. 3: (Color online) The ratios of J/ψ production as a function of p_T at forward rapidity in $p + p$ collisions (a) and y integrated over all p_T (b) relative to CT10 for CTEQ5M (blue dashed), CTEQ6M (red dot-dashed) and MSTW (magenta dot-dot-dot-dash-dashed).

differ. By employing the same value of F_c for all the sets, the differences in magnitude as well as shape are emphasized.

The CTEQ5M distribution, higher than the other gluon densities at the J/ψ scale for $x < 0.01$, results in a 20% larger overall cross section. This manifests itself at low p_T where the integral difference is 32% and, most prominently, in the rapidity distribution around $y \sim 0$ where it is $\sim$ 50% higher. The CTEQ5M gluon distribution, as already noted, takes a constant value for $x < 10^{-5}$. The rapidity distribution for the PDF is consequently narrower than the other three shown. The corresponding p_T distributions do not reflect the $x < 10^{-5}$ behavior because, in the rapidity range illustrated, the low p_T J/ψ's are at higher x values, see the $y = 4$ line in Fig. 1(a).

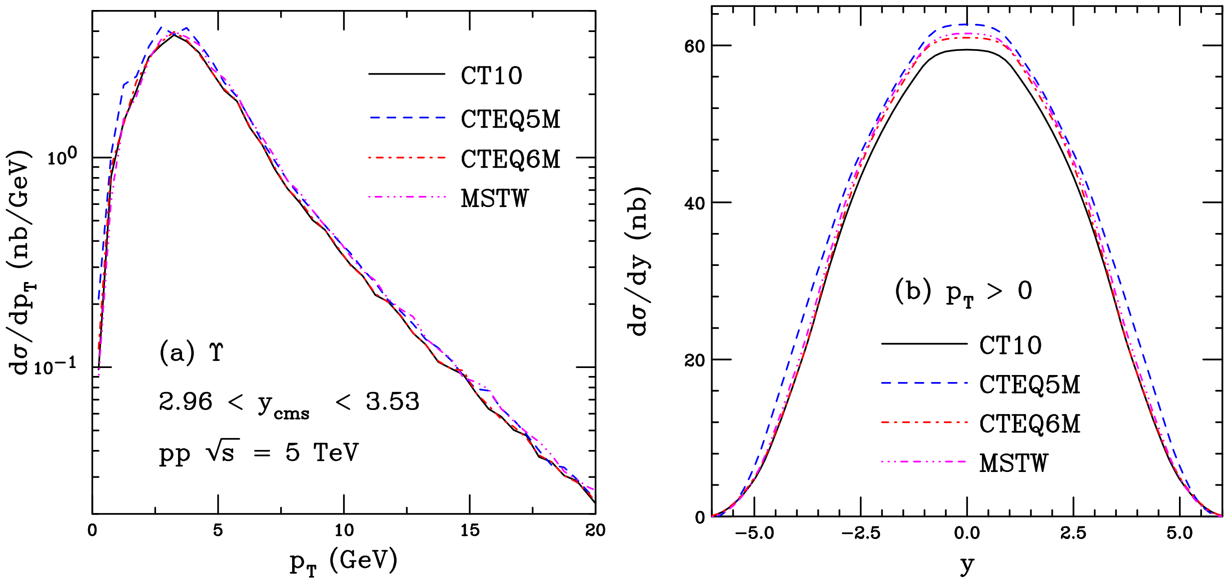

FIG. 4: (Color online) The Υ distribution at forward rapidity in $p+p$ collisions (a) and the p_T-integrated y distribution (b). Results from CT10 (black solid), CTEQ5M (blue dashed), CTEQ6M (red dot-dashed) and MSTW (magenta dot-dot-dot-dash-dashed) are compared, all calculated with the same input parameters and using the same value of F_C as for CT10.

The similarity of the CT10 and CTEQ6M gluon distributions results in very similar p_T and y distributions. The MSTW set gives a 15% lower cross section for the J/ψ with most of the difference at low p_T. The rapidity distributions are also slightly narrower than CT10 but less than that of the CTEQ5M calculation.

Figure 3 presents the ratios of the CTEQ5M, CTEQ6M and MSTW calculations to the CT10 results as a function of p_T and y. Aside from the lowest p_T bins, the ratios in Fig. 3(a) are practically independent of p_T except for CTEQ5M which seems to show slow growth with p_T after a strong drop at $p_T < 5$ GeV. For $5 < p_T < 30$ GeV, the ratios to CT10 all agree within 10%. The CTEQ6M result differs from CT10 by $\sim 2\%$ for $p_T > 5$ GeV. The p_T-integrated rapidity distributions in Fig. 3 are all quite different. While the CTEQ6M result is within 5% of that of CT10 over all rapidity, the other ratios are narrower. Note that the $p_T > 0$ ratio in Fig. 3(b) is larger than the ratio at $p_T > 5$ GeV in 3(a) because the y distribution is dominated by low p_T. The sharp drop for CTEQ5M is where $x \sim 10^{-5}$. Since the MSTW gluon distributions do not have the same behavior, they are broader than CTEQ5M but the ratio is less than 0.7.

The corresponding Υ results are displayed in Figs. 4 and 5. The larger factorization scale makes the results all very similar in magnitude for this case with the integrated cross sections differing by less than 10%, even for CTEQ5M. The ratios as a function of p_T are all relatively flat, especially between CTEQ6M and CT10. The largest difference among the results appears at large rapidities where there is a sudden increase in the ratio for $|y| \sim 5$, dropping off afterward where $x \sim 10^{-5}$ is reached for Υ production.

The rapidity distributions have been shown to be more dependent on the chosen baseline proton parton densities than the p_T distributions. This arises because of the differing behavior of the low x gluon densities. Due to the larger scale, the dependence on the proton parton densities is less important for the higher mass Υ.

IV. COLD NUCLEAR MATTER EFFECTS

To go beyond $p+p$ collisions, the proton parton densities must be replaced by those of the nucleus. If A is a nucleus, the nuclear parton densities, $f_i^A(x_2,\mu^2)$, can be assumed to factorize into the nucleon parton density, $f_i^p(x_2,\mu^2)$, independent of A; and a shadowing ratio, $S^i_{\rm P,S}(A,x_2,\mu^2)$ that parameterizes the modifications of the nucleon parton densities in the nucleus. The centrality dependence will be discussed elsewhere [7] so here $S^i(A,x_2,\mu^2)$ alone is addressed. (Note that only x_2 is mentioned here since only one nuclear beam is employed. In Pb+Pb collisions, the distributions as a function of x_1 would also be modified.)

No other cold matter effects are considered in this paper because the goal is to determine how far the data can be described by the assumption of shadowing alone. However, since lower energy J/ψ production clearly requires some

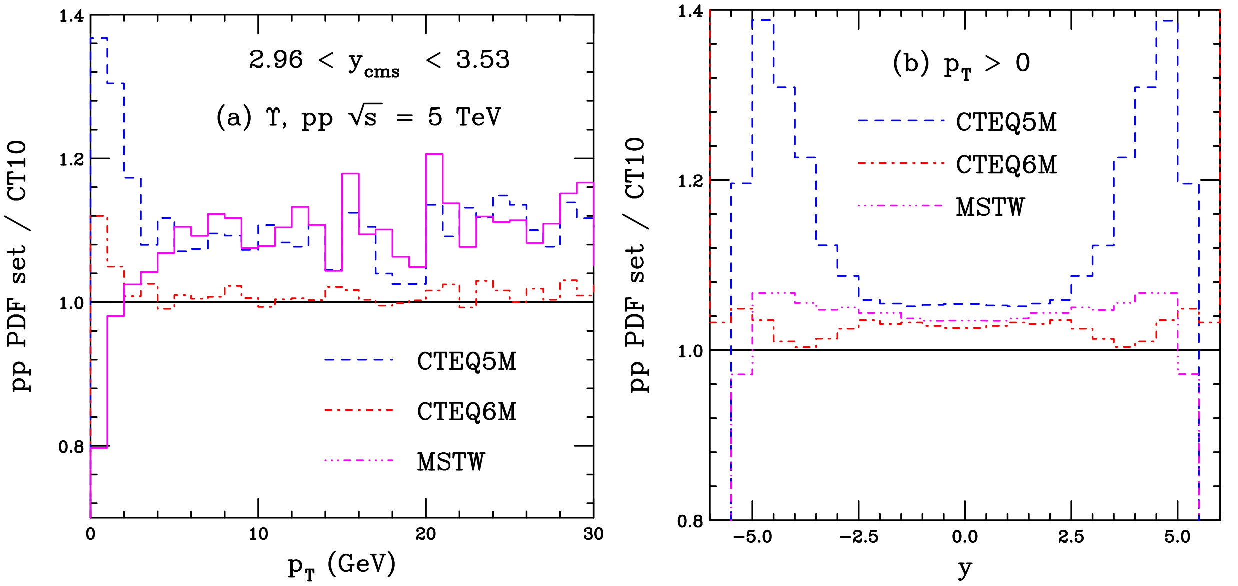

FIG. 5: (Color online) The ratios of Υ production as a function of p_T at forward rapidity in $p+p$ collisions (a) and y integrated over all p_T (b) relative to CT10 for CTEQ5M (blue dashed), CTEQ6M (red dot-dashed) and MSTW (magenta dot-dot-dot-dash-dashed).

effects beyond shadowing, these are briefly mentioned here.

At fixed-target energies, the x_F dependence clearly shows that shadowing is not the only contribution to the J/ψ nuclear dependence as a function of Feynman $x_F = 2p_z/\sqrt{s}$ for the final-state particle [47, 48]. Indeed, the characteristic decrease of $\alpha(x_F)$ (in $d\sigma_{pA}/dx_F = (d\sigma_{pp}/dx_F)A^{\alpha(x_F)}$) for $x_F \geq 0.25$ cannot be explained by shadowing alone [49]. In fact, the data so far suggest approximate scaling with x_F, not the target momentum fraction x_2 [50]. The PHENIX J/ψ data are consistent with an increase of effective 'absorption' at forward rapidity, as discussed in Ref. [6], similar to that seen in fixed-target experiments at large x_F [51]. The results for shadowing alone are compared with the PHENIX data at the end of this paper.

Effects not considered here which affect the forward rapidity region in particular are energy loss in cold matter and intrinsic charm. The effect of energy loss, both with and without including shadowing, has been discussed in detail in Ref. [52, 53]. However, given the rather simple power law dependence employed for the $p+p$ distribution, it would be worth pursuing embedding this approach within a production model such as the CEM. Intrinsic charm is not considered here because the interesting region, $x_F \geq 0.25$, is inaccessible for quarkonium production in $|y| \leq 5$, see Ref. [8].

Absorption by nucleons or comovers, which could affect the entire rapidity region, are not included in this paper. The effective J/ψ absorption cross section has been seen to decrease with energy at midrapidity [54]. When shadowing is included, the $\sqrt{s}$ dependence is somewhat stronger due to the increased shadowing effect at low x [54]. If the nuclear crossing time is shorter than the J/ψ formation time, the effective absorption decreases with $\sqrt{s_{NN}}$ as the state remains small during the entire time it spends in the target. However, absorption may play a role at the most backward rapidities when the quarkonium state is slow and can convert from the pre-resonance state to the final-state J/ψ in the target [6, 55]. The Υ(1S) absorption cross section is expected to be smaller than that of the J/ψ because of its smaller radius.

While the J/ψ-comover cross section is smaller than the nucleon absorption cross section, comovers may be more important for the excited charmonium and bottomonium states. (While these states have larger radii than the ground state quarkonium, this does not affect their potential absorption by nucleons since they still pass through the nuclear matter in their pre-resonant state.) Strong differences between the J/ψ and ψ' $R_{\rm dAu}$ at RHIC as a function of collision centrality [56] would support the importance of comovers since their density increases with centrality. Recent comover-based p+Pb calculations show that this interpretation is consistent with the data [57].

V. NUCLEAR MODIFICATIONS OF THE PARTON DENSITIES

Several parameterizations of the nuclear modifications in the parton densities (nPDFs) are employed to probe the possible range of shadowing effects: EPS09 [38], EKS98 [43, 44], nDS and nDSg [46], and the two FGS sets, FGS-H and FGS-L [40]. Since gg processes dominate quarkonium production over all measurable rapidities at the LHC, the behavior of the nuclear gluon parton densities is highlighted in this section. The main results in this paper are obtained with EPS09 NLO to make a fully consistent NLO calculation with the NLO CEM cross sections. However, in the following section, the differences between the nPDF sets and between their LO and NLO manifestations on J/ψ and Υ production in p+Pb collisions at $\sqrt{s_{_{NN}}} = 5$ TeV are discussed in more detail.

All these sets involve some data fitting, typically nuclear deep-inelastic scattering (nDIS) data with additional constraints from other observables such as Drell-Yan dimuon production. The fact that these sets also include Drell-Yan production and do not include initial-state energy loss in matter in their global analyses, they exclude the possibility of additional quark energy loss since incorporating both over counts the effect on the sea quark densities. (Of course, if energy loss is generated by gluon emission either from an initial-state gluon or from the produced $Q\overline{Q}$ pair, there is no energy loss possible in the Drell-Yan process, $q\overline{q} \to l^+l^-$, since a virtual photon generates a lepton pair.) None of these data provide any direct constraint on the nuclear gluon density. It is thus obtained through fits to the μ^2 dependence of the nuclear structure function, F_2^A, and the momentum sum rule. The useful perturbative μ^2 range of the nDIS data is rather limited since these data are only available at fixed-target energies. Thus the reach in momentum fraction, x, is also limited and there is little available data for $x < 10^{-2}$ at perturbative values of μ^2. This situation is likely not to improve until an eA collider is constructed [58]. The various sets of nuclear modifications are discussed in order of their release.

The EKS98 parameterization, by Eskola and collaborators [43, 44], available for $A > 2$, is a leading order fit using the GRV LO [42] proton parton densities as a baseline. The first EKS98 fits [43] used the GRV LO proton densities from 1992 [42]. This set employed a starting scale of $\mu_0^2 = 0.3$ GeV. The set eventually released as EKS98 was constructed with CTEQ4L [41] with initial scale of $\mu_0 = 1.6$ GeV. To match the starting scale of the EKS98 nPDF set, the CTEQ4L distributions were backward evolved from $\mu = 1.6$ GeV to 1.5 GeV [44]. They checked that the nPDF results from these two proton PDFs were consistent even though the proton PDFs themselves were quite different: the GRV LO set employed a valence-like gluon distribution at the starting scale, $xg(x, \mu_0^2) \sim x^\alpha P(x)$ where $\alpha > 0$ and $P(x)$ is a polynomial function, while CTEQ4L takes $\alpha < 0$, giving $xg(x, \mu_0^2)$ a finite value as $x \to 0$. The minimum scales of the two sets are also very different. The kinematic range of EKS98, the only leading order set considered since no NLO set was obtained at the time, is $1.5 \leq \mu \leq 100$ GeV and $10^{-6} \leq x < 1$. All the sets produced by Eskola and collaborators are based on piecewise functions at the minimum scale of the set that include small x shadowing, antishadowing at intermediate x, an EMC region (named for the effect first identified by the European Muon Collaboration) with $R_g < 1$ at larger x and Fermi motion as $x \to 1$.

deFlorian and Sassot produced the nDS and nDSg parameterizations [46] at both leading and next-to-leading order for $4 < A < 208$. Their results were based on the GRV98 proton PDFs at LO and NLO [45], using the same starting scales as GRV98, $\mu_{0\,\mathrm{LO}}^2 = 0.40$ GeV, and $\mu_{0\,\mathrm{NLO}}^2 = 0.25$ GeV. GRV98 assumed valence-like input for the sea quarks and gluons at the minimum scales with $xc(x, \mu_0^2) = 0$. The GRV98 gluon densities are not significantly different at low x when evolved to higher scales. The leading order set has a somewhat higher gluon density at low x [45]. Of the two deFlorian and Sassot sets, nDS and nDSg, the first, nDS, is an unconstrained fit that gives the best fit, χ^2. To provide a set with stronger gluon shadowing, they constrained a second fit to give $S_g^{\mathrm{Au}} \equiv 0.75$ at $x = 0.001$ and $\mu^2 = 5$ GeV^2. This set, nDSg, was a much poorer fit to the New Muon Collaboration (NMC) and SLAC nDIS data and the E772 Drell-Yan cross sections [46].

They showed that their results for the suppression factor for π^0 production at RHIC, $R_{\mathrm{dAu}}^{\pi^0}(p_T)$, at both LO and NLO were in agreement with each other [46]. This should be the case for a consistent order-by-order extraction of the nPDFs: not that the shadowing ratios are similar but that they give similar observable results, such as the nuclear suppression factors. The kinematic reach in x is the same as EKS98 while the μ^2 range is larger, $1 < \mu^2 < 10^6$ GeV^2.

The FGS sets by Frankfurt, Guzey and Strikman take the highest initial scale of all the nPDF sets, $\mu = 2$ GeV [40]. They only provide NLO sets. Instead of a general global analysis, their nPDFs are based on the leading-twist approximation and rely on the diffractive PDFs. The Gribov-Glauber approach employed naturally introduces a centrality dependence for the shadowing. Their baseline proton parton densities are the CTEQ5M distributions. Therefore, their extraction is only good for $x > 10^{-5}$.

They extracted two sets to represent an upper and a lower bound on the shadowing ratios. FGS-H is gives stronger shadowing based on the two-nucleon scattering cross section. FGS-L is based instead on the πN scattering cross section. Since this is larger than the two-nucleon scattering cross section, the shadowing effect derived in this case is weaker. Their approach is only applicable for $x < 0.1$. For $x > 0.1$, the sea quark ratio relative to the nucleon is fixed to unity and gluon antishadowing is obtained through the momentum sum rule. Hence, in this high x region, the two parameterizations are identical. Their approach does not allow predictions for shadowing on the valence quark

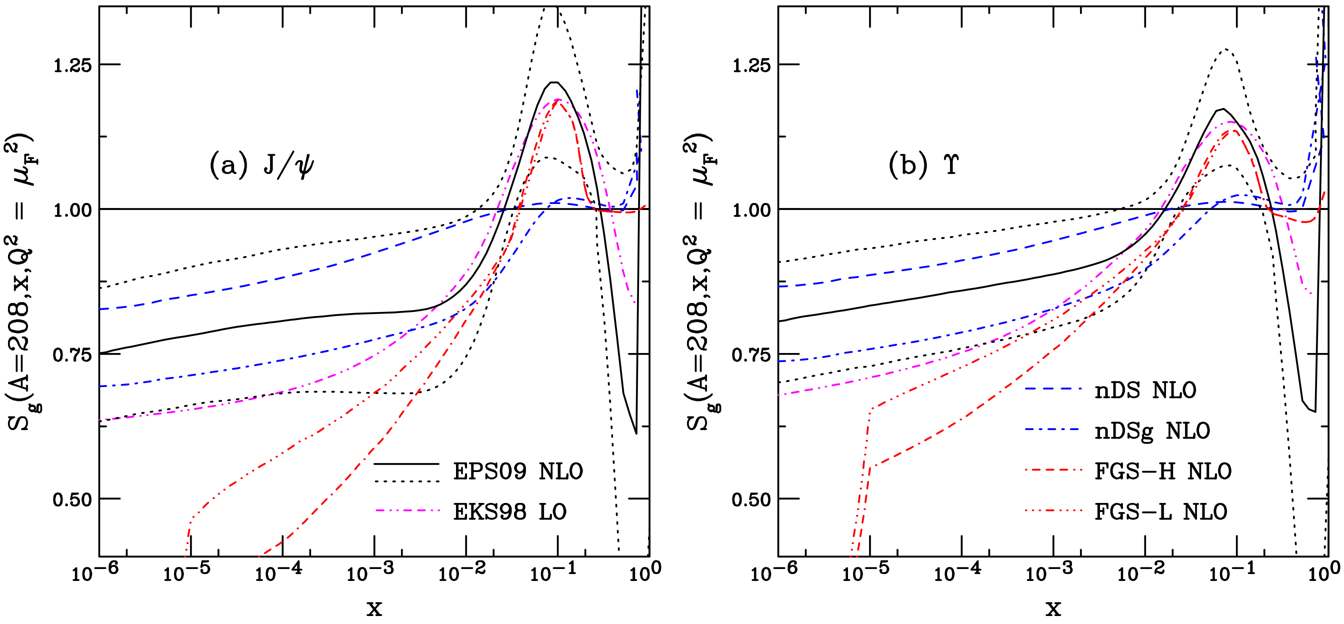

FIG. 6: (Color online) Gluon shadowing ratios calculated for Pb nuclei ($A = 208$) calculated at the central value of the fitted factorization scales for J/ψ (a) and Υ (b). The EPS09 NLO set is shown by the black solid curve while the uncertainty band is outlined by the black dotted curves. The NLO nDS and nDSg parameterizations are given in the blue dashed and dot-dashed curves respectively. The LO EKS98 parameterization is given in the magenta dot-dot-dash-dashed curve. The NLO FGS-H and FGS-L results are given by the red dot-dash-dash-dashed and dot-dot-dot-dashed curves respectively.

distributions, these are taken from the LO EKS98 set. The FGS sets are available only for some specific nuclei where diffractive data exist: ^{12}C, ^{40}Ca, ^{110}Pd, ^{197}Au and ^{208}Pb. The sets are valid in $10^{-5} < x < 0.95$ and $2 < \mu < 100$ GeV.

The EPS09 [38] LO and NLO parameterizations included uncertainties on the global analyses, both at LO and NLO, by varying one of the 15 fit parameters within its extremes while holding the others fixed. The upper and lower bounds on EPS09 shadowing are obtained by adding the resulting uncertainties in quadrature [38]. The EPS09 central LO results are in quite good agreement with the older EKS98 parameterization. The EPS09 LO sets are based on the CTEQ61L densities which are nearly flat at the initial scale as $x \to 0$. The EPS09 NLO densities are based on the CTEQ6M densities. Starting with CTEQ6M, a valence-like shape for the gluon distribution was adopted at the starting scale, in this case the charm mass threshold of $\mu_0 = 1.3$ GeV [36]. The EPS09 sets assume the same starting scale as the CTEQ6 sets and is valid in the range $10^{-6} < x < 1$ [38].

Figure 6 shows the sets discussed in this section at the scales of J/ψ (a) and Υ (b) production. The results are shown for x values as low as 10^{-6}. The EPS09 NLO sets are shown in the black solid and dotted curves. The solid curves show the central results while the dotted curves outline the NLO bands. The EPS09 results for J/ψ show a change in curvature, almost a dip, at $x \sim 0.01$, with a small rise at lower x followed by an eventual decrease. There is a rather strong antishadowing peak from $0.02 < x < 0.2$ where the ratio drops below unity again, in the EMC region.

The EKS98 LO ratio is similar to that of the central EPS09 LO set but decreases more smoothly, giving a stronger shadowing at lower x than the NLO set, a 40% shadowing effect at $x = 10^{-6}$ rather than the 30% effect at NLO. At the lowest x values, the central EPS09 LO is equivalent to the lower limit of the EPS09 NLO band.

The FGS-H and FGS-L sets are similar to the others but are somewhat narrower in the antishadowing region. However, they decrease faster with decreasing x than any of the other sets shown. They drop sharply at $x = 10^{-5}$. Instead of either fixing the ratio at its value at $x = 10^{-5}$, as in the CTEQ5M proton PDF set, or trying to make a smooth extrapolation to lower x, it simply falls off more like a step function.

The nDS set has somewhat stronger shadowing that the upper limit of the EPS09 NLO band while the nDSg set is between the EPS09 NLO central and lower limits. These sets, of all the results shown, have no antishadowing at all.

The same features can be observed for the shadowing ratios at the Υ scale. The EPS09 band now decreases more smoothly as x decreases. The FGS-H ad FGS-L ratios show the steep drop at the limit where $x = 10^{-5}$ more clearly at the larger scale. All the slopes of the other nPDF sets become rather similar.

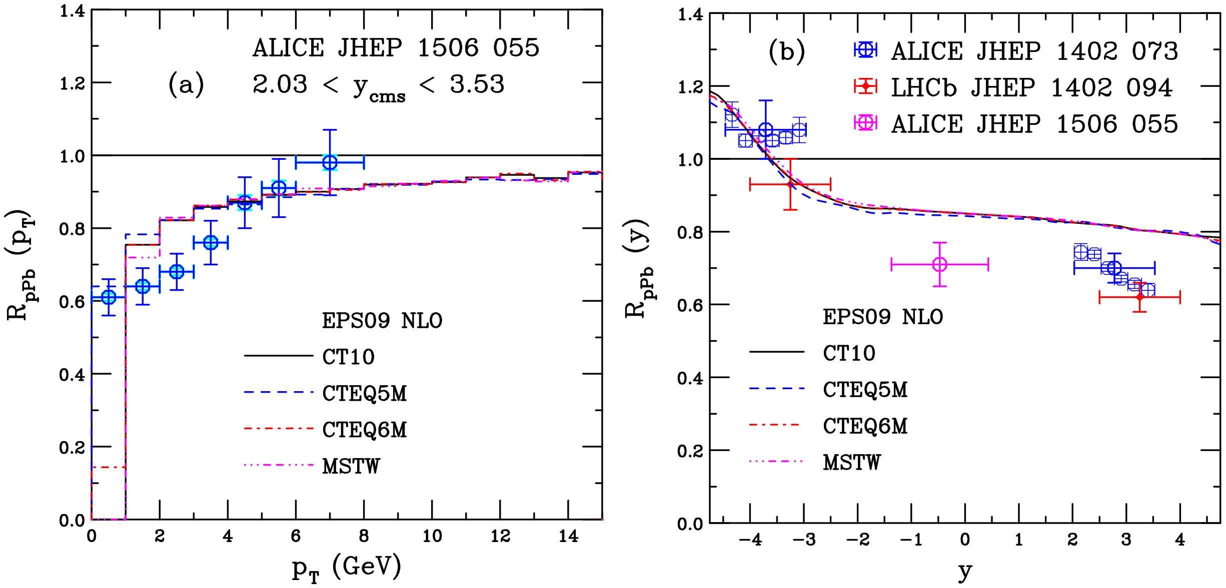

FIG. 7: (Color online) The J/ψ ratio $R_{p\rm Pb}(p_T)$ for ALICE at forward rapidity [2] (a) and p_T-integrated $R_{p\rm Pb}(y)$ from ALICE [1, 2], $|y| > 0$ in the blue points and midrapidity in magenta, and LHCb [4] (red points) (b) are given. The ratios are shown for CT10 (black solid), CTEQ5M (blue dashed), CTEQ6M (red dot-dashed) and MSTW (magenta dot-dot-dot-dash-dashed).

VI. RESULTS

Calculations of the J/ψ and Υ production ratios, $R_{p\rm Pb}$ and R_{FB} as a function of rapidity and p_T, are shown taking only nuclear shadowing effects into account. First, results with the same shadowing parameterization calculated with different proton PDFs are compared in Sec. VI A. These results are shown for the J/ψ only and compared to a subset of the available data. In the remainder of this section, the calculations are compared to the full J/ψ and Υ data sets from ALICE and LHCb. The measurements are compared to the EPS09 NLO uncertainty bands in Sec. VI B. Next, the leading and next-to-leading order shadowing results of EPS09 and nDS are compared and contrasted in Sec. VI C. Thereafter, the results from the nPDF sets shown in Fig. 6 are compared to the data and each other in Sec. VI D. The mass and scale uncertainties on the central EPS09 set are compared to the uncertainties in the shadowing parameterizations themselves in Sec. VI E. Next how well the $A + A$ results factorize into a product of $p + A$ and $A + p$ collisions is discussed in Sec. VI F. Finally, the EPS09 NLO uncertainty bands are presented for the RHIC kinematics in Sec. VI G.

A. Comparison of EPS09 NLO for Different Proton PDFs

To begin, the dependence of the shadowing results on the chosen set of proton parton distributions is checked. As demonstrated in Sec. III B, the choice of proton PDF has a strong effect on the shape of the individual $p + p$ distributions. Since each shadowing parameterization is based on different proton PDFs, it is necessary to find out if this also changes the shape of the nuclear suppression factors. The central EPS09 NLO set is employed for this study.

The results for $R_{p\rm Pb}(p_T)$ and $R_{p\rm Pb}(y)$ are shown in Fig. 7. The left hand side shows $R_{p\rm Pb}(p_T)$ for the ALICE forward rapidity bin, $2.03 < y_{\rm cms} < 3.53$ while the right-hand side displays the p_T-integrated $R_{p\rm Pb}(y)$. The only visible difference between the results is for the lowest p_T bin shown, $1 < p_T < 2$ GeV, where the difference is $\sim 4\%$ between the ratios with CTEQ5M and MSTW relative to CT10. There is no difference in the CT10 and CTEQ6M ratios. At higher p_T, the difference is negligible. Some variation on the order of the percent level is seen as a function of rapidity, particularly in the backward region. Since these variations are significantly less than those between the nPDFs themselves, The choice of proton PDF has a negligible effect on the results.

B. EPS09 NLO Uncertainties

Here the EPS09 NLO uncertainties in J/ψ and Υ production are presented. The calculated nuclear suppression factor, $R_{p\rm Pb}$, and the forward-backward ratio, R_{FB}, are compared to the ALICE and LHCb data.

1. J/ψ

Figure 8 compares the suppression factors for $J/\psi \to \mu^+\mu^-$ as a function of p_T at forward (a) and backward (b) rapidity as well as for $J/\psi \to e^+e^-$ at midrapidity (c). The rapidity dependent ratio is shown in (d). The solid curves show the EPS09 NLO central results while the dashed curves outline the upper and lower limits of the EPS09 NLO uncertainty band. In all cases, the bands on the EPS09 NLO uncertainties are obtained by adding the differences in the results obtained by varying each parameter separately by one standard deviation of the fit in quadrature.

In general, the p_T-dependent data are in relatively good agreement with the EPS09 NLO bands, if not with the central values themselves. In the forward region, the measured $R_{p\rm Pb}$ is compatible with the lower edge of the uncertainty band for $p_T < 6$ GeV. The data at backward rapidity also suggest a somewhat stronger cold matter effect, compatible with the upper edge of the band. While the uncertainties on the data at midrapidity are larger than those on the calculation, the data again indicate a somewhat stronger effect than suggested by EPS09 NLO. However, within the uncertainties of both the data and the calculations, the results are, in general agreement.

A similar conclusion can be drawn from the p_T-integrated rapidity dependence. The ALICE data at forward and backward rapidity are shown in two ways: a single p_T-integrated point over the entire rapidity acceptance and with each broad y bin broken up into six separate bins. While the smaller bins are almost independent of y in the backward region, there is a decrease in $R_{p\rm Pb}(y)$ in the forward region. The overall observed dependence of $R_{p\rm Pb}(y)$ is in good agreement with the p_T-dependent results in Fig. 8(a)-(c). While the LHCb are within one standard deviation of the ALICE data, they are somewhat lower.

As discussed previously, the suppression factor $R_{p\rm Pb}$ is somewhat artificial since there is currently no $p+p$ reference measurement at the same energy as the p+Pb data. Instead the reference is obtained from an interpolation between the $p+p$ measurements at 2.76 and 7 TeV, as described in Sec. II. The forward-backward ratio reduces the systematic uncertainty.

The results are compared to the J/ψ calculations in Fig. 9. Note that the uncertainties on the ratio are narrower than those of the forward and backward regions separately, as shown in Fig. 8. The uncertainty bands are formed by taking the forward-backward ratios for each of the 31 EPS09 sets individually and then adding the uncertainties in quadrature. The calculated ratios are almost independent of p_T. This behavior is due to the fact that the forward ratio is less than unity and increasing with p_T while the backward ratio is greater than unity over most of the p_T range. The data instead show a minimum at low p_T, increasing to $R_{p\rm Pb} \sim 0.8$ at $p_T \sim 8$ GeV, albeit with large statistical uncertainties.

The calculated ratios as a function of rapidity are very narrow for $y < 2.5$ before broadening at larger y. This behavior is obvious from looking at $R_{p\rm Pb}(y)$ since, for $y > -2.5$ the uncertainty band is parallel to the central value and almost linear so that when the forward-backward ratio is formed, the band is compressed. The ratio $R_{FB}(y)$ broadens and decreases at $y > 3$, where, at backward y, $R_{p\rm Pb}(y)$ enters the antishadowing region. The forward-backward ratio narrows again at $y \sim 4$, near the 'pinch' in $R_{p\rm Pb}(y)$, where the data are best constrained, and finally broadens again in the antishadowing regime where the constraints are poorer. The data are below the calculated band because, while the backward region is rather well described, the central value is above the data at forward rapidity. While the ALICE $R_{FB}(y)$, in a smaller rapidity range, is almost flat, the LHCb ratio varies more. However, in the bin where the rapidity ranges of the two experiments overlap, they are in good agreement.

Finally the recent ATLAS forward-backward measurement of $R_{FB}(p_T)$ in the central region, $|y_{\rm cms}| < 1.94$ and $R_{FB}(y)$ for $8 < p_T < 30$ GeV [16] is briefly described. Their results are consistent with unity in both p_T and y and agree well with the EPS09 NLO calculations. The results shown in Fig. 9(a) are in the forward region while the ATLAS measurement is at midrapidity. Given the higher scale implicit in the p_T range covered by ATLAS, as well as the higher x in the rapidity range covered by ATLAS, it is unsurprising that the EPS09 NLO result is consistent with unity here. Similarly, given that the EPS09 NLO result integrated over p_T in Fig. 9(b) is already similar to unity for $|y| < 1.5$, the same ratio for $p_T > 8$ GeV can be expected to have a more shallow slope and deviates less from unity than the results compared to ALICE and LHCb here.

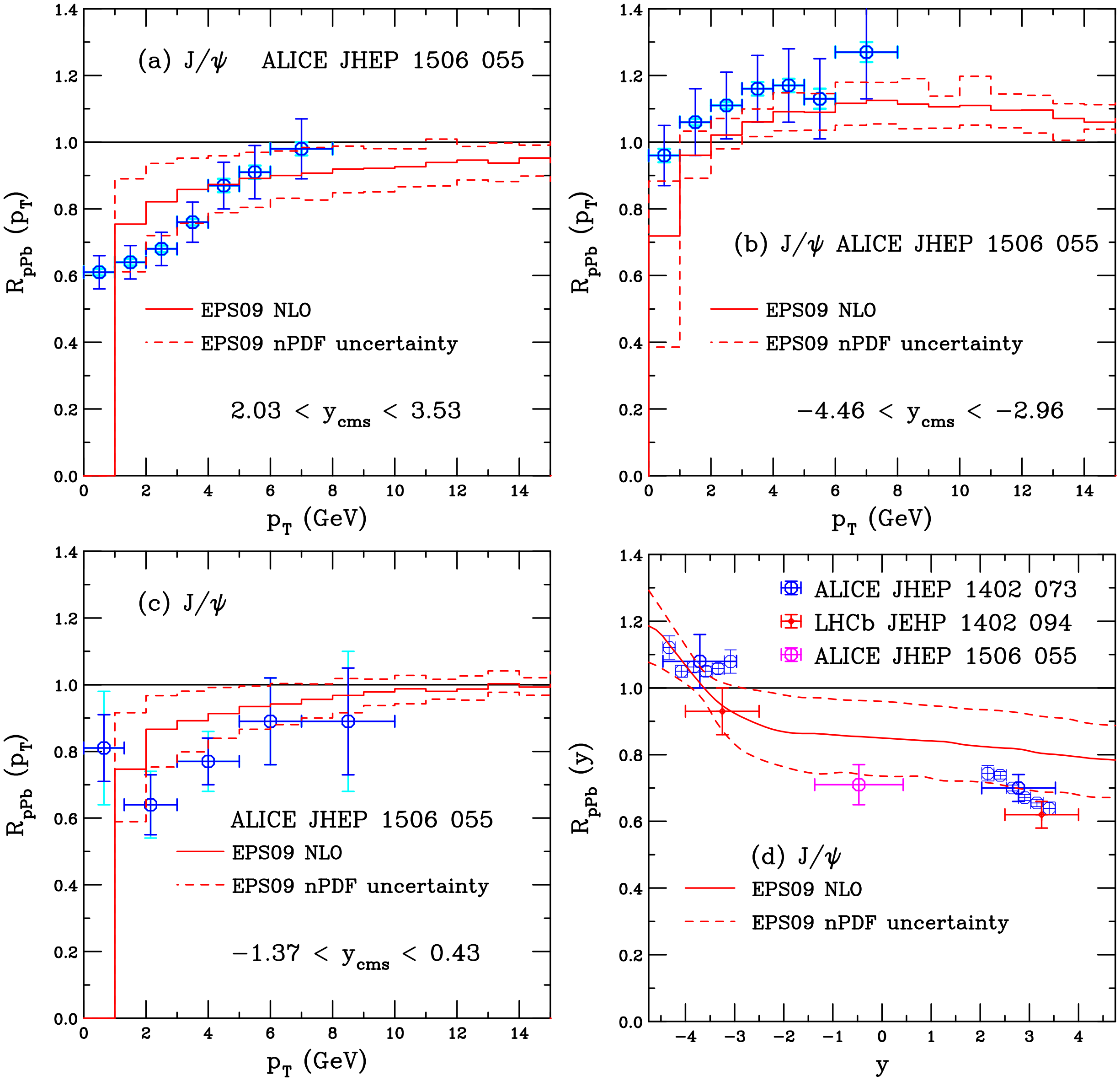

FIG. 8: (Color online) The J/ψ ratio $R_{p\rm Pb}(p_T)$ in the ALICE acceptance at forward (a), backward (b) and central (c) rapidity [2]. In (d), the ALICE results on $R_{p\rm Pb}(y)$ [1, 2] are given, $|y| > 0$ in the blue points and midrapidity in magenta, along with those of LHCb [4] (red points). The EPS09 NLO uncertainty band is shown.

2. Υ

The results for the Υ suppression factor, $R_{p\rm Pb}$, are shown in Fig. 10. In this case, the data are insufficient to form $R_{p\rm Pb}(p_T)$ or $R_{FB}(p_T)$. In addition, no midrapidity e^+e^- Υ measurement has been reported. It is also not possible to separate $R_{p\rm Pb}(y)$ into smaller bins due to the low statistics. Finally, the ALICE and LHCb Υ data, in the forward and backward rapidity bins, while within one standard deviation of each other, do not appear to be in very good agreement with each other. Therefore, it is more difficult to draw conclusions about the Υ results.

The p_T-dependent ratios differ from those for J/ψ most at low p_T. In particular, the backward rapidity region shows an antishadowing effect already at low p_T. At higher p_T values, the scales are similar since $p_T > m$ in both cases. The EPS09 NLO uncertainty band is somewhat narrower, especially as a function of rapidity, where the ALICE and LHCb Υ data are both shown. The agreement with the LHCb data is quite good while the agreement with ALICE is rather poor. The two data sets are approximately within one standard deviation of each other but LHCb is indicative of antishadowing at the approximate rapidity of the EPS09 NLO antishadowing peak while the ALICE result is not.

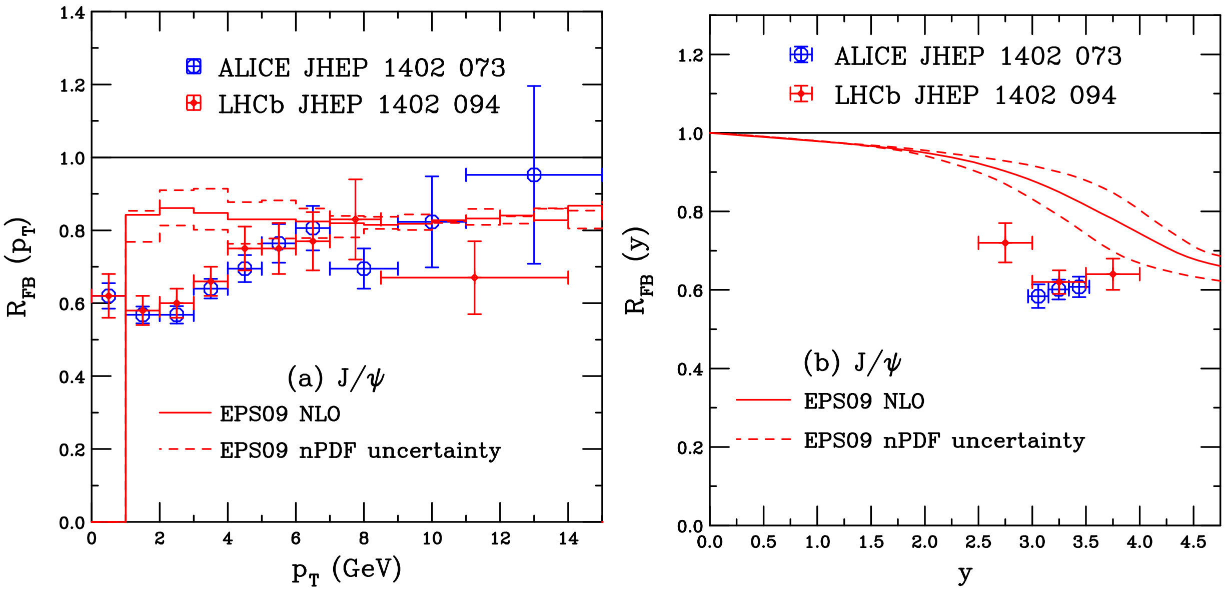

FIG. 9: (Color online) The J/ψ forward-backward ratio $R_{FB}(p_T)$ in the ALICE overlap region, $2.96 < y_{\rm cms} < 3.53$ (a) and $R_{FB}(y)$ (b). The EPS09 NLO uncertainty band is shown with the ALICE [1] (blue) and LHCb [4] (red) data.

At forward rapidity, the ALICE J/ψ and Υ results for $R_{p{\rm Pb}}$ are similar.

The Υ forward-backward ratio is shown in Fig. 11. The p_T-dependent ratio is lower than that of J/ψ due to the greater Υ antishadowing. The uncertainty is larger because the uncertainty on the backward rapidity J/ψ $R_{p{\rm Pb}}$ is narrower than for Υ since the ALICE J/ψ region is near the 'pinch' between the shadowing and antishadowing regions while the Υ rapidity is directly in the region where the uncertainties are larger for gluons. This is also reflected by the rapidity dependence.

C. Comparison of Leading and Next-to-Leading Order Results

Previously it was reported that the shadowing parameterizations gave the same results for the LO and NLO cross sections [59]. That result was based, however, on employing the LO EKS98 set in the LO and NLO CEM calculations. In addition, other authors have suggested that the order of the calculation does not matter and NLO nPDF sets can be used with LO quarkonium calculations. It is worth checking these assumptions in detail.

As discussed in the previous section, the nDS and nDSg LO and NLO sets were checked for consistency for the PHENIX π^0 data [46]. The same check is now performed for J/ψ and Υ production as a function of rapidity for EPS09 LO and NLO and for nDS and nDSg LO and NLO in Fig. 12.

The shadowing parameterizations are compared in Fig. 12 (a) and (b). There are considerable differences between the EPS09 bands at $x < 0.01$. The NLO result has a different curvature than the LO one, changing slope and becoming flatter, decreasing slowly as x is lowered. On the other hand the LO bands decrease smoothly. There is, however, very little difference in the upper limit of the band, with the weakest shadowing effect. The difference is more pronounced for the central sets and striking for the lower limit of the band, with the strongest shadowing. In this case, the lower NLO limit is close to the central EPS09 LO set. There is also some difference between the nDS and nDSg parameterizations. While the difference is essentially negligible for the nDS set, there is a stronger deviation between the nDSg curves, particularly around $x \sim 0.01$. For $x < 0.002$, the ratios are parallel.

Whether these differences affect $R_{p{\rm Pb}}(y)$ for quarkonium production is now discussed. The EPS09 LO calculation is made with a fully LO CEM calculation in $2 \to 1$ kinematics. The NLO calculation is with the NLO matrix elements in the CEM.

Results are shown for in Fig. 12 (c) and (d). There is clearly a strong effect for EPS09 with the central LO result passing through the ALICE and LHCb data while only the lower limit of the NLO band reaches the data, an ap+proximate 15% difference between the two results. However, the nDS and nDSg results, while clearly not on top of each other, as they are for the π^0 calculation [46], agree within $\sim 3\%$.

Why is one derivation nearly consistent order by order and the other is not? The primary cause is likely the

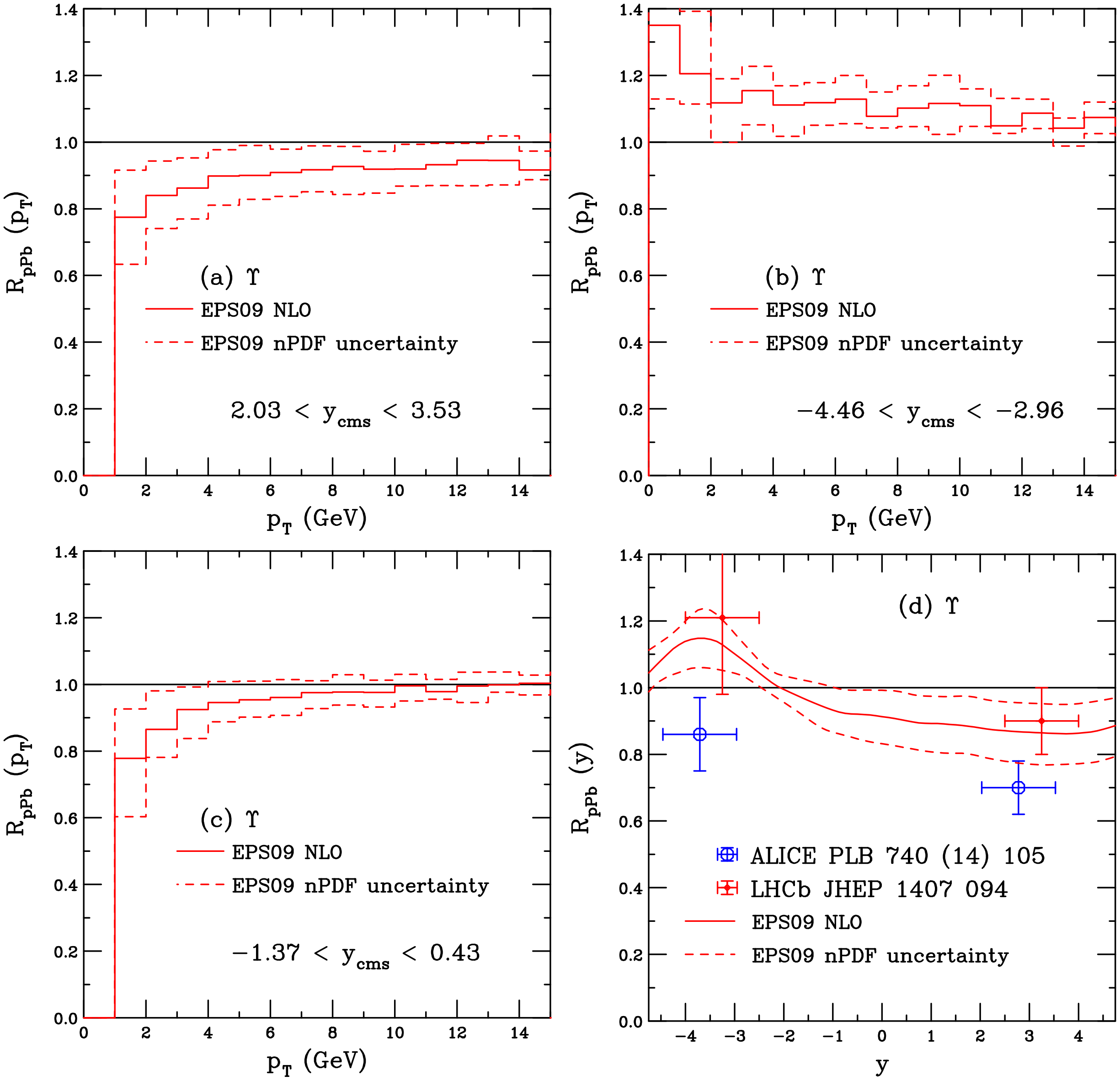

FIG. 10: (Color online) The Υ ratio $R_{p\mathrm{Pb}}(p_T)$ in the ALICE acceptance at forward (a), backward (b) and central (c) rapidity. The ratio $R_{p\mathrm{Pb}}(y)$ from ALICE [3] (blue) and LHCb [?] (red) is shown in (d). The EPS09 NLO uncertainty band is shown.

low x behavior of the baseline proton parton densities, as already mentioned in Sec. V. The CTEQ6M, GRV98 LO and GRV98 NLO gluon distributions are all based on valence-like initial distributions at μ_0, $x^\alpha P(x)$. However, the CTEQ61L gluon density takes an almost constant finite value at μ_0^2, *i.e.* $\alpha \sim 0$. This initial difference carries forward over all μ^2 because the NLO set must have stronger μ^2 evolution to fit the same sets of DIS data as at LO. Thus the CTEQ6M distribution evolves much more rapidly in μ^2 than does CTEQ61L. At the factorization scale of Υ production, the difference between CTEQ6M and CTEQ61L is still substantial while the GRV98 LO and NLO gluon distributions, with similar starting behavior, are closer together. The EPS09 LO shadowing thus has to be stronger at low x to produce the same behavior at higher scales as the EPS09 NLO shadowing. The compensation does not have to be as large for the nDS sets since the GRV98 LO and NLO sets are more similar at low x and the scale relevant for quarkonium production.

The agreement between the EPS09 LO and NLO results is not improved for the higher scale of Υ production, as shown in Fig. 12 (e) and (f). The higher scale, as already noted, weakens the shadowing and narrows the uncertainty bands but does not bring the central results at LO and NLO into better agreement. This conclusion is likely independent of the specific final state as long as its production is dominated by low x gluons.

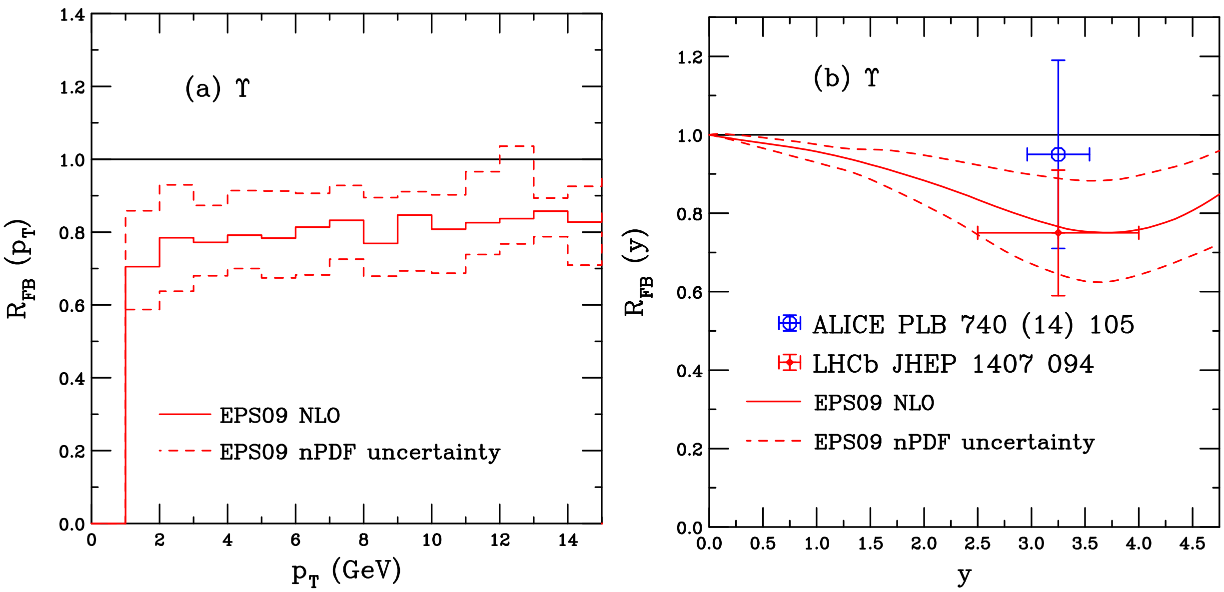

FIG. 11: (Color online) The Υ forward-backward ratio $R_{FB}(p_T)$ in the ALICE overlap region (a) and $R_{FB}(y)$ (b). The EPS09 NLO uncertainty band is shown, along with the ALICE [3] (blue) and LHCb [5] (red) data.

There are, however, valid reasons for there to be a few percent difference between the LO and NLO results seen with nDS and nDSg. The LO CEM calculation is a $2 \to 1$ process with fixed values of x_1 and x_2 for a given y since there is no p_T scale in the calculation, only in the factorization scale which can be adjusted to include an average value of p_T. The NLO calculation, on the other hand, includes $2 \to 2$ and $2 \to 3$ processes (the LO+virtual and real contributions respectively) to the NLO CEM result. The NLO CEM calculation does not have a fixed correspondence between x_1, x_2 and y because of the p_T scale. This higher scale can also lead, on average, to a larger factorization scale and a somewhat larger x_2 on average in the NLO calculation. All these differences can cumulatively lead to the $2-3\%$ effect between LO and NLO observed for the nDS sets. Similar arguments can also explain the differences between the LO CEM and LO CSM [60] results and are not directly attributable to the production mechanism per se.

D. Comparison of Shadowing Parameterizations

In this section, the central EPS09 NLO results are compared to those with other shadowing parameterizations.

1. J/ψ

Figures 13 and 14 compare the NLO nDS, nDSg, FGS-H and FGS-L results to the central EPS09 NLO result (shown in black). The results with the EKS98 LO set are also shown. In the p_T ratios, the EPS09 central set tends to underestimate the effect relative to the data except at backward rapidity. Indeed, at forward and midrapidity, the nDS set is the only one that underestimates the data more since it has the weakest gluon shadowing. At backward rapidity, the nDS result is close to unity over all p_T while nDSg exhibits some shadowing. This is because these two sets have no gluon antishadowing. At forward rapidity, the FGS-H and FGS-L sets result in the strongest effect, significantly stronger than the data in the case of FGS-H. The set that comes closest to agreement with the data in all three rapidity regions is EKS98 which only overestimates the shadowing effect for $p_T > 6$ GeV.

In all cases the p_T-dependent results for all the nPDF sets shown agree within 10% for $p_T > 10$ GeV. This can be expected because the evolution of the modifications is relatively strong for the gluons.

As seen in Fig. 13(a), the spread between predictions is largest in the forward region where the shadowing predictions differ most. Indeed, in the p_T bin centered at 1.5 GeV, there is a factor of ~ 8 between the values of $R_{p\mathrm{Pb}}$. The gap is reduced to ~ 1.3 by $p_T \sim 3.5$ GeV. The weakest p_T dependence is given by the calculations with nDS and the central EPS09 NLO set. The nDSg set also results in a weak p_T dependence but has a stronger overall shadowing effect. The

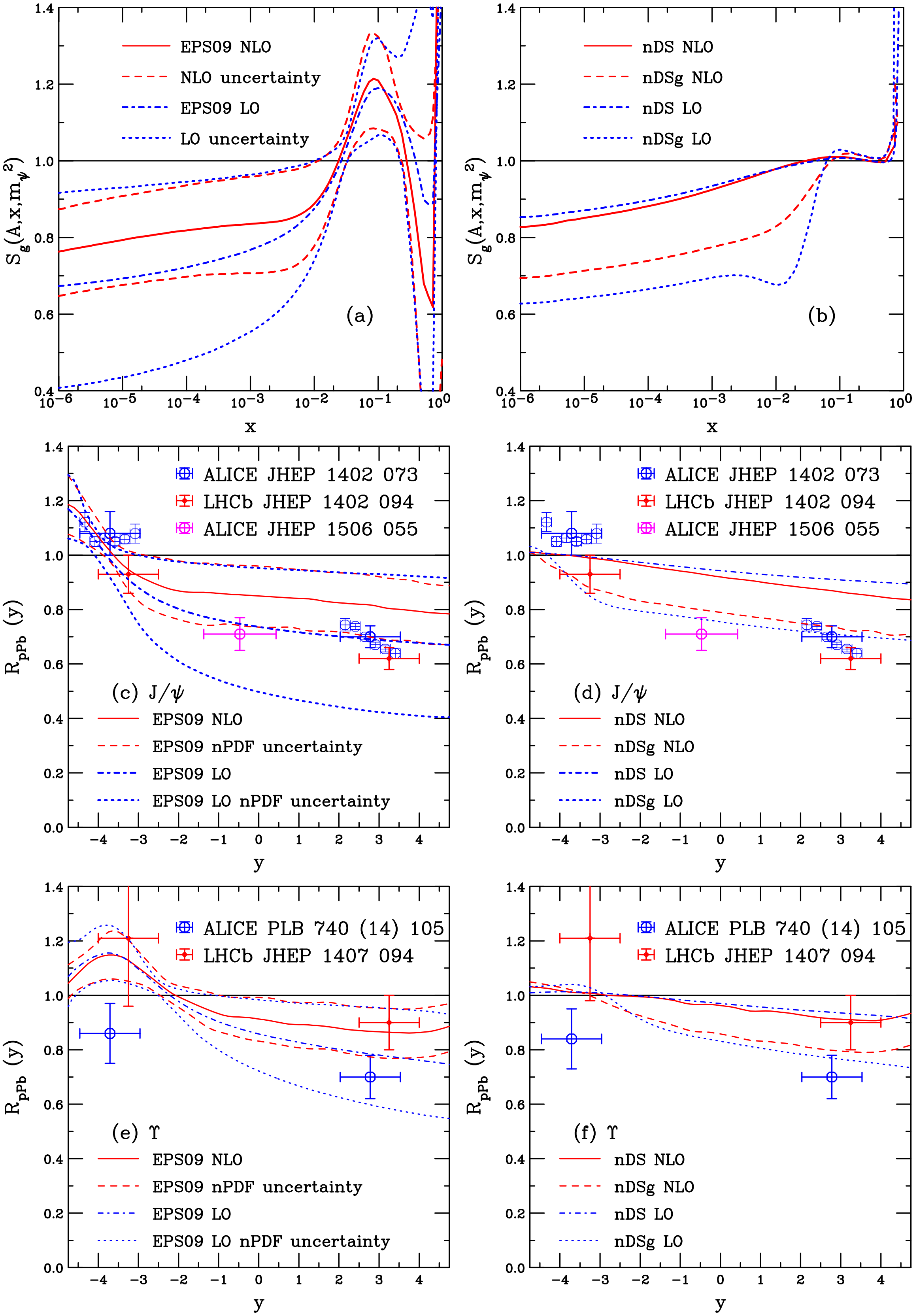

FIG. 12: (Color online) The EPS09 central results, as well as the uncertainty bands, are shown in (a), (c) and (e). In all cases, the solid red curve shows the central NLO result while the dashed red curves delineate the NLO uncertainty band. The dot-dashed blue curve is the LO central result while the dotted curves outline the LO uncertainty band. The nDS and nDSg results are presented in (b), (d) and (f). The red solid curves show the NLO nDS result while the dashed red curves are the

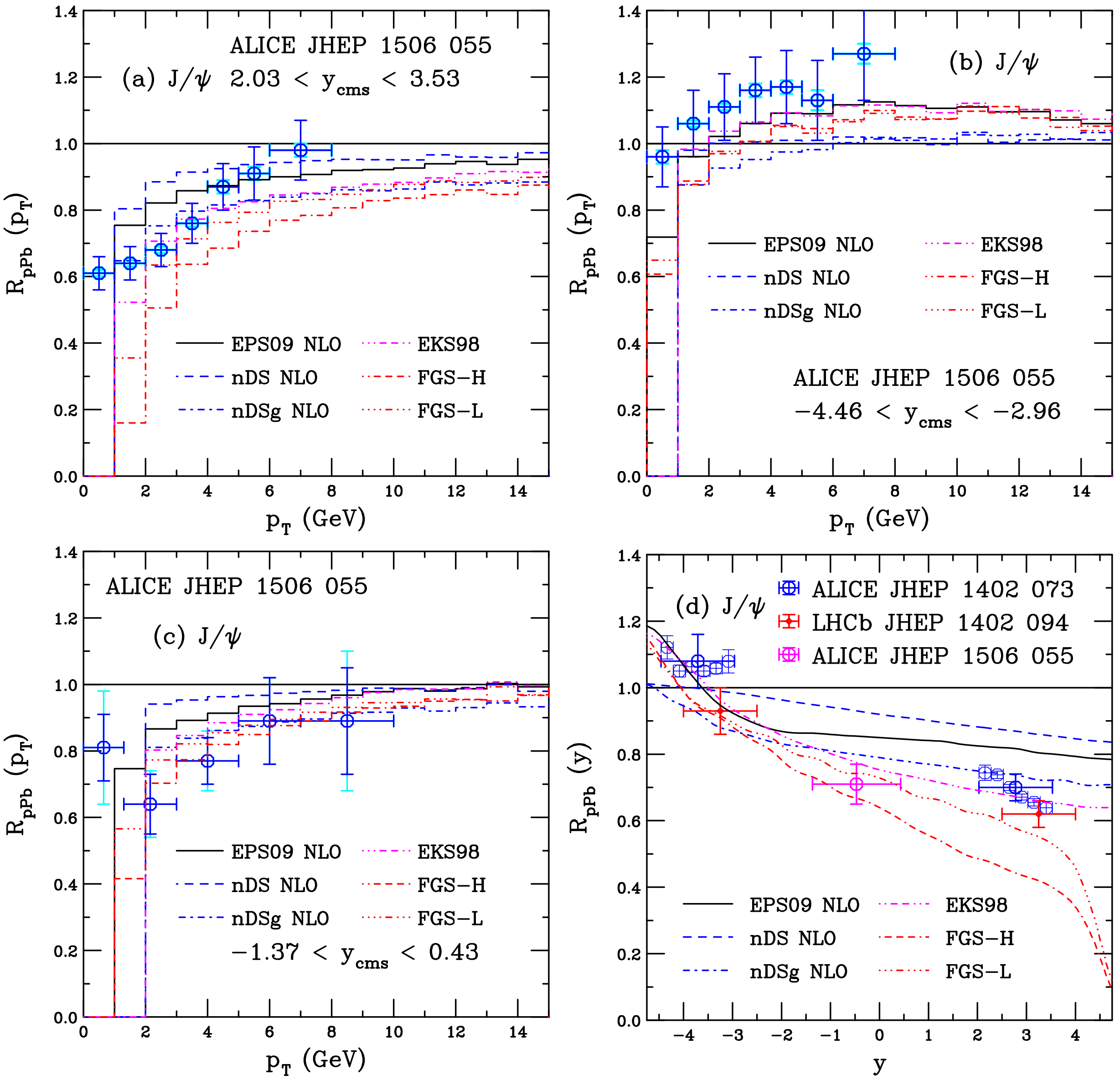

FIG. 13: (Color online) The J/ψ ratio $R_{p\mathrm{Pb}}(p_T)$ in the ALICE acceptance at forward (a), backward (b) and central (c) rapidity [2]. In (d), the ALICE results on $R_{p\mathrm{Pb}}(y)$ [1, 2] are given, $|y| > 0$ in the blue points and midrapidity in magenta, along with those of LHCb [4] (red points). The results are shown for central EPS09 NLO (black), nDS NLO (blue dashed), nDSg NLO (blue dot-dashed) and EKS98 LO (magenta dot-dot-dash-dashed), FGS-H (red dot-dash-dash-dashed) and FGS-L (red dot-dot-dot-dash).

strongest shadowing comes from the FGS sets which overpredict the shadowing strength. The best agreement with the ALICE data is obtained for the EKS98 LO set which has no NLO counterpart. Note that the measured $R_{p\mathrm{Pb}}$ approaches unity at $p_T \sim 7$ GeV while none of the shadowing parameterizations give a result approaching unity over the entire p_T range shown.

In the backward region, illustrated in Fig. 13(b), the results show some antishadowing, except for nDS and nDSg which specifically exclude it. All the calculations lie below the centroids of the data, partly because the ALICE acceptance is centered on the side of the antishadowing peak so that the calculated antishadowing is, on average, lower than that of the data. Note also that the antishadowing peak is broad in p_T, with some antishadowing remaining at $p_T \sim 15$ GeV.

The p_T-dependent results from the nPDF sets come closest together in the midrapidity bin, with a spread of at most 30%, as seen in Fig. 13(c). Although the data again suggest stronger shadowing at midrapidity than the calculations,

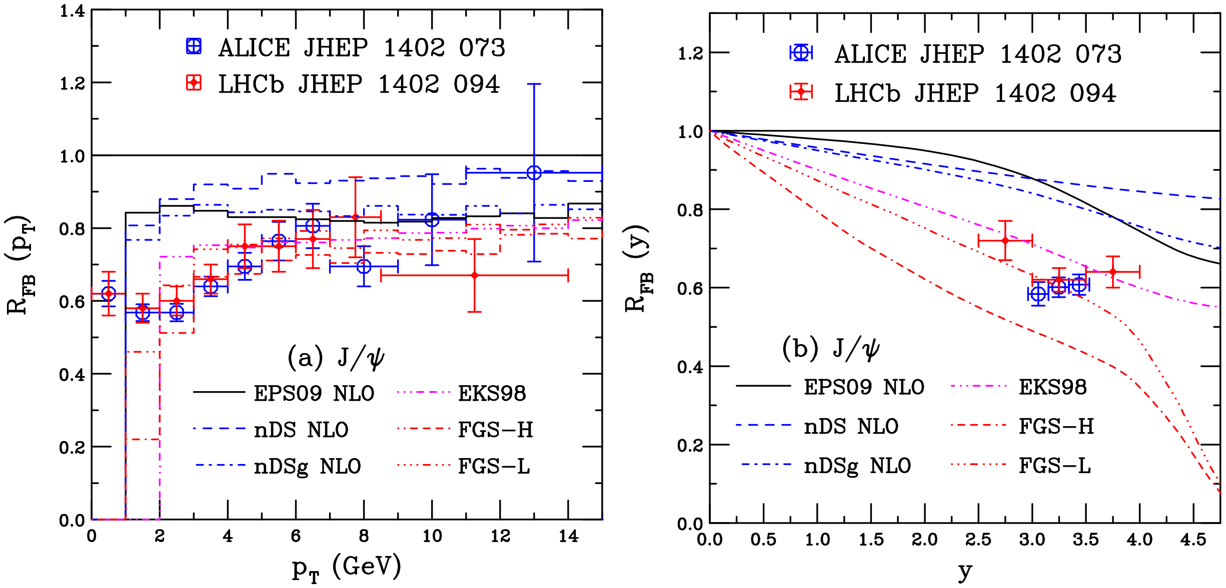

FIG. 14: (Color online) The J/ψ forward-backward ratio $R_{FB}(p_T)$ in the ALICE overlap region (a) and $R_{FB}(y)$ (b). The data from ALICE [1] (blue) and LHCb [4] (red) are shown. The ratios are for central EPS09 NLO (black), nDS NLO (blue dashed), nDSg NLO (blue dot-dashed) and EKS98 LO (magenta dot-dot-dash-dashed), FGS-H (red dot-dash-dash-dashed) and FGS-L (red dot-dot-dot-dash).

the uncertainties in the data are large since the number of J/ψ in this bin are lower by more than a factor of 100 than in the forward and backward bins, see Table I. In this rapidity range, the shadowing effect is reduced to less than 10% for $p_T > 10$ GeV with all sets.

The largest difference in the $R_{p\mathrm{Pb}}$ ratios is as a function of rapidity, shown in Fig. 13(d), since the p_T-integrated ratios access the lowest x values. The ratios are closest at backward rapidity, not surprisingly, because the EPS09 NLO and EKS98 sets follow each other closely for $x > 0.002$, see Fig. 6(a). Since the FGS sets are somewhat narrower in the antishadowing x region, this is manifested as an apparent shift toward negative rapidity in the antishadowing peak for the J/ψ. The EPS09 NLO and EKS98 are in closest agreement with the integrated ALICE rapidity bin which is larger than unity. The ALICE data were split into six smaller bins in both the forward and backward rapidity bins. In the backward region, the smaller bins are almost independent of rapidity which is not consistent with any of the shadowing results. Since the LHCb backward rapidity result is below unity, only the nDS result is not in agreement with LHCb.

The ratios separate further in the shadowing regions at mid and forward rapidity. Since the ALICE p_T-integrated ratio at midrapidity is almost the same as that at forward rapidity, albeit with somewhat larger uncertainty, the midrapidity point is only in agreement with the FGS-L and FGS-H sets. This is not surprising: because of their steep drop at low x, they show stronger shadowing than EKS98 already at $x \sim 0.001$ and considerably overestimate the effect at forward rapidity where $x < 10^{-5}$. In the forward bin, the EKS98 and nDSg results are in best agreement with the ALICE and LHCb results. The ALICE forward bin, when split into smaller bins, shows a linear dependence on rapidity but with a slope steeper than any of the shadowing calculations. Overall the EKS98 parameterization, one of the oldest and LO only, agrees best with the data. Since it is similar in shape to the EPS09 LO central set, shown in Fig. 12(a), this is not surprising. The EPS09 LO and EKS98 sets, based on CTEQ61L and CTEQ4L respectively, are the only sets of those from EPS09 and nDS that are not based on valence-like gluon distributions in the proton and are thus subject to slower scale evolution.

In Fig. 14, the forward-backward ratios are shown as functions of p_T and y. The EPS09, nDS and nDSg ratios are nearly independent of p_T, thus above the data over most of the p_T range. The EKS98 and FGS sets have a somewhat stronger dependence on p_T and thus agree more closely with the forward-backward ratio at low p_T. However, of these, only the FGS-L and EKS98 sets are in agreement with the rapidity-dependent ratio. All the sets, with the exception of the central EPS09 NLO set, give forward-backward ratios that are linear in y. As already discussed this is due to the abrupt change in slope of EPS09 NLO at $x \sim 0.002$, see Fig. 6(a), at the transition from shadowing to antishadowing, absent from the other sets shown.

Overall, the EKS98 LO set seems to agree best with the J/ψ data, both $R_{p\mathrm{Pb}}$ and R_{FB}. This is somewhat less

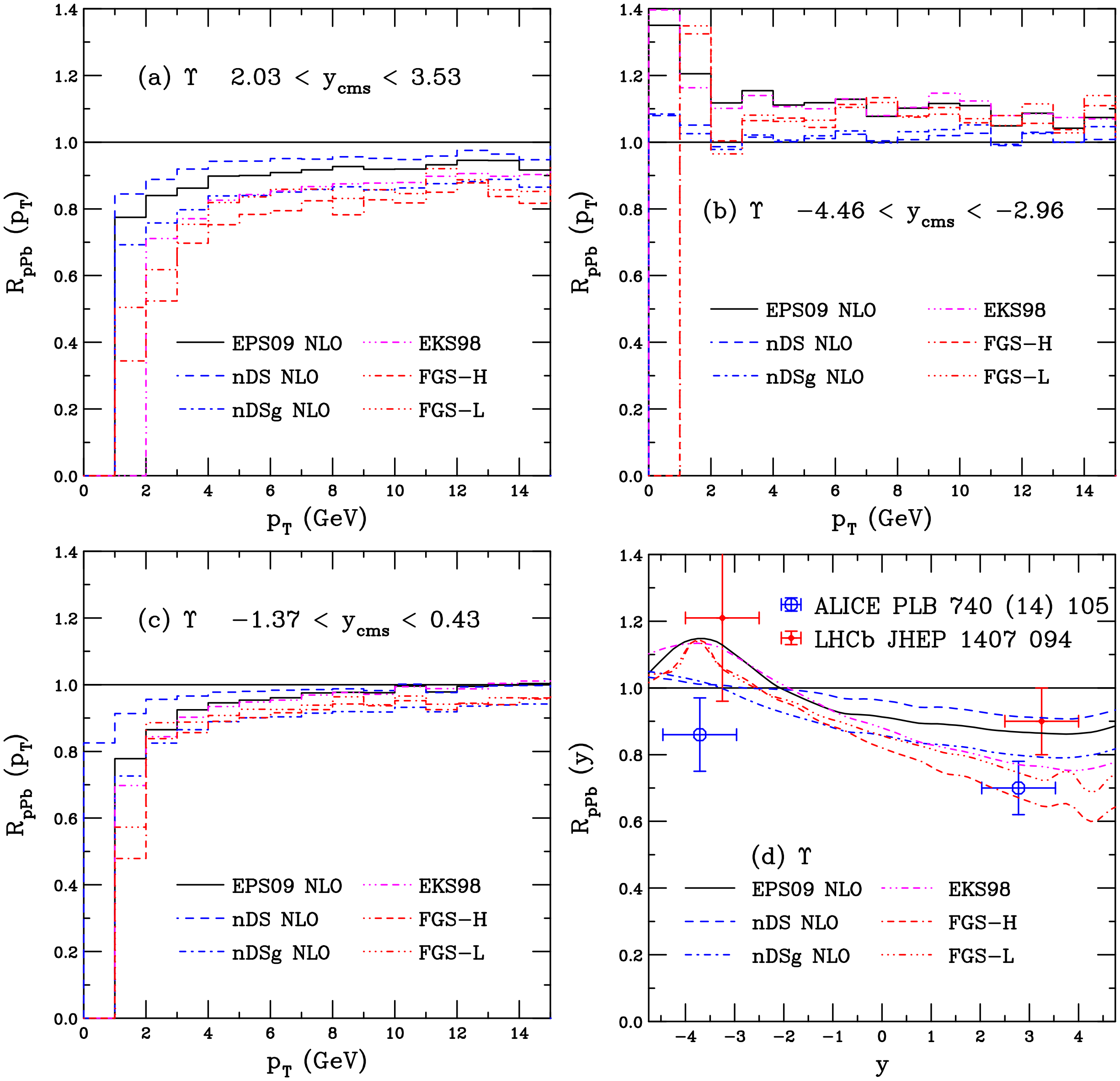

FIG. 15: (Color online) The Υ ratio $R_{p\rm Pb}(p_T)$ in the ALICE acceptance at forward (a), backward (b) and central (c) rapidity. The ratio $R_{p\rm Pb}(y)$ is compared to the ALICE [3] (blue) and LHCb [5] (red) data in (d). The ratios are for central EPS09 NLO (black), nDS NLO (blue dashed), nDSg NLO (blue dot-dashed) and EKS98 LO (magenta dot-dot-dash-dashed), FGS-H (red dot-dash-dash-dashed) and FGS-L (red dot-dot-dot-dash).

than satisfying since a LO nPDF set is used with a NLO cross section calculation. In addition, it is one of the older sets employed here. However, it agrees rather well with EPS09 LO when calculated with LO matrix elements, even though the baseline proton PDF and its behavior at low x is very different. It was previously demonstrated that the ratio $R_{pA}(y)$, calculated at LO and NLO with the EKS98 LO set, gave almost identical results at each order [59]. This is not a surprise since the gg contribution dominates production both at LO and NLO and the shift in x and μ^2 due to the different scales is small when integrated over p_T.

2. Υ

Figures 15 and 16 present the results for Υ production in the same rapidity ranges. The p_T-dependent $R_{p\rm Pb}$ ratios shown in Fig. 15(a)-(c) exhibit somewhat less spread than the counterpart J/ψ calculations. The main difference is

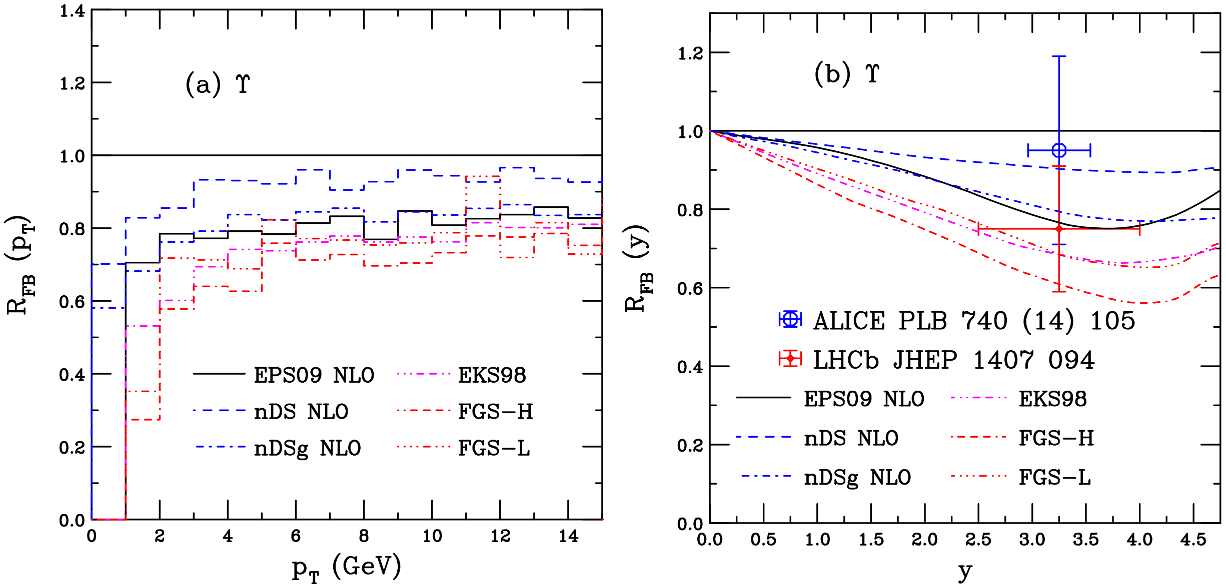

FIG. 16: (Color online) The Υ forward-backward ratio $R_{FB}(p_T)$ in the ALICE overlap region (a) and $R_{FB}(y)$ (b). The ALICE [3] (blue) and LHCb [5] (red) data are shown in (b). The ratios are shown for central EPS09 NLO (black), nDS NLO (blue dashed), nDSg NLO (blue dot-dashed) and EKS98 LO (magenta dot-dot-dash-dashed), FGS-H (red dot-dash-dash-dashed) and FGS-L (red dot-dot-dot-dash).

that now, at the higher scale and correspondingly larger x probed, the antishadowing peak for Υ production is fully within the acceptance of ALICE and LHCb in the backward direction. Thus $R_{p\mathrm{Pb}}(p_T) > 1$ over all p_T in Fig. 15(b) with $R_{p\mathrm{Pb}}(p_T \sim 1.5\,\mathrm{GeV}) \sim 1.2$.

The rapidity-dependent ratio, $R_{p\mathrm{Pb}}(y)$, shown in Fig. 15(d) echoes the low p_T results. Even the nDS and nDSg ratios are above unity in the backward rapidity region, albeit in the backward edge of the experimental acceptance. This is because, in the high-x region, these sets become large as $x \to 1$ with the turn on of this effect beginning at $x \sim 0.5$ and the region of $x \sim 0.1$ is where the gluon distribution becomes larger than unity. Note that even though the FGS gluon ratios are only somewhat narrower than the EPS09 NLO ratio for the same scale, see Fig. 6(b), for the actual Υ calculation shown here, the difference is enhanced. At backward rapidity, the sets are in agreement only with the higher LHCb point while they all miss the ALICE point at $R_{p\mathrm{Pb}}(y) < 1$. At forward rapidity, the results spread more. The strongest shadowing is again with the FGS results but due to the larger x probed for the Υ, the $x < 10^{-5}$ region is not entered in the rapidity range shown although it is approaching the edge of this region, contributing to the fluctuations in the FGS curves in Fig. 15(d). As for the J/ψ, the EKS98 slope is more linear for $y > -1$ than than the EPS09 NLO central value. Thus the nDS and nDSg results, with weak shadowing, as well as the EPS09 NLO results agree best with the weaker shadowing reported by LHCb while the FGS results generally agree better with the stronger shadowing reported by ALICE. The EKS98 LO parameterization is between the two measurements and also includes antishadowing. Therefore, it gives the best overall result for this measurement given the quality of the currently available data.

The forward-backward ratios for Υ production are shown in Fig. 16. None of the results for the various nPDF sets exhibit a strong p_T dependence. The FGS and EKS98 results are generally below those of EPS09 NLO over all p_T while those of nDS and nDSg are higher. These rather flat ratios can be attributed to the relative p_T-independence for $p_T > 4$ GeV for $R_{p\mathrm{Pb}}(p_T)$ in Fig. 15(a) and (b) while the stronger shadowing and antishadowing, respectively, in these regions at $p_T < 4$ GeV essentially give the same forward-backward ratio as at higher p_T.

The rapidity dependence of the forward-backward ratio, Fig. 16(b), is similar for all the nPDF sets even though the magnitude of the effect varies. Because all the ratios increase above unity in the backward direction, the ratios all decrease almost linearly, except for EPS09 NLO, with a minimum at $3.5 \leq y \leq 4.0$. While most of the ratios rise again at larger rapidity, the nDS and nDSg ratios only flatten with rapidity above $y \sim 3.5$.

In summary, of all the nPDFs, the LO EKS98 set agrees best with the currently available data. However, this is a rather unsatisfying conclusion because the LO set is used in a NLO calculation. Even if the x values do not strongly differ between LO and NLO, the LO shadowing parameterization should be a stronger function of x, with a larger overall shadowing magnitude, to produce the same $R_{p\mathrm{Pb}}$ ratios order by order, as was previously shown to be the case for the nDS and nDSg sets. A re-evaluation of the nPDF analysis, including appropriate LHC data, should be made in order to resolve the issue.

E. Mass and Scale Dependence

In this section, the mass and scale dependence of the shadowing ratios are discussed, using the EPS09 NLO set as an example. Similar results are expected for the other nPDFs but EPS09 NLO is chosen because the shadowing uncertainty can be compared to that of the mass and scale. Recall that for charm-J/ψ $(m, \mu_F/m, \mu_R/m) = (1.27 \pm 0.09\,\mathrm{GeV}, 2.1^{+2.55}_{-0.85}, 1.6^{+0.11}_{-0.12})$ is employed while for bottom-Υ production, $(m, \mu_F/m, \mu_R/m) = (4.65 \pm 0.09\,\mathrm{GeV}, 1.4^{+0.77}_{-0.49}, 1.1^{+0.22}_{-0.20})$ is used.

The uncertainties of the EPS09 NLO nPDF sets compared to those of the mass and scale uncertainties on $d\sigma/dp_T$ for the J/ψ are illustrated in Fig. 17. Here the ALICE p_T distributions in p+Pb collisions [2] are compared to the NLO CEM calculations. The red solid and dashed curves are the central EPS09 NLO results with the uncertainty band due to the EPS09 parameter variations. This band is rather narrow on the scale of the plots with the only clear separation between the curves at low p_T where the shadowing effects are largest. Clearly, a 20-40% effect on $R_{p\mathrm{Pb}}(p_T)$ on a linear scale in this region results in a narrow band on the p_T distribution itself on a logarithmic scale. The lowest p_T results are not shown because the underlying $p+p$ calculation does not accurately numerically cancel the divergences in the negative weight Monte Carlo [22]. The intrinsic k_T kick used to obtain the shape of the p_T distribution in the low-p_T region was fixed at RHIC energies and successfully compared to the J/ψ p_T distributions at $\sqrt{s} = 7$ TeV [13].

The magenta curves in Fig. 17 show the uncertainty due to the mass and scale variations. The mass and scale uncertainties are calculated based on results using the one standard deviation uncertainties on the quark mass and scale parameters. If the central, upper and lower limits of $\mu_{R,F}/m$ are denoted as C, H, and L respectively, then the seven sets corresponding to the scale uncertainty are $\{(\mu_F/m, \mu_F/m)\} = \{(C,C)$, (H,H), (L,L), (C,L), (L,C), (C,H), $(H,C)\}$. The uncertainty band can be obtained for the best fit sets by adding the uncertainties from the mass and scale variations in quadrature. The envelope containing the resulting curves,

$$d\sigma_{\max}/dX = d\sigma_{\mathrm{cent}}/dX + \sqrt{(d\sigma_{\mu,\max}/dX - d\sigma_{\mathrm{cent}}/dX)^2 + (d\sigma_{m,\max}/dX - d\sigma_{\mathrm{cent}}/dX)^2}\,, \tag{5}$$

$$d\sigma_{\min}/dX = d\sigma_{\mathrm{cent}}/dX - \sqrt{(d\sigma_{\mu,\min}/dX - d\sigma_{\mathrm{cent}}/dX)^2 + (d\sigma_{m,\min}/dX - d\sigma_{\mathrm{cent}}/dX)^2}\,, \tag{6}$$

defines the uncertainty on the cross section where X can be either p_T or y. The EPS09 uncertainty band is based on the mass and scale set with the central mass value and $(\mu_F/m, \mu_F/m) = (C,C)$.

In Fig. 17, the mass and scale uncertainties are clearly significantly larger than those of the shadowing parameterizations alone, still a factor of ~ 2 on the J/ψ p_T distributions over a wide p_T range. Thus, even though the uncertainties on the J/ψ cross section in the CEM are reduced relative to those calculated previously, see Ref. [13], they are still significantly larger than those of shadowing on the central mass and scale values. One would naively expect the uncertainties on $R_{p\mathrm{Pb}}$ and R_{FB} to reflect the results shown in Fig. 17 but, as will be shown, it depends on the method used to calculate the uncertainty.

Several methods of estimating the size of the mass and scale uncertainty on the ratios are proposed. These are described before comparing to the data. Note that all of these calculations are based on the EPS09 NLO central set rather than making a global nPDF + mass + scale uncertainty by calculating the 30 error sets for EPS09 with the 8 additional mass and scale combinations that define the mass and scale uncertainty on the cross section for $p+p$ and p+Pb.

The most naive, labeled $m/\mu_F/\mu_R\,v1$ on Figs. 18-22, is to take the ratios of p+Pb to $p+p$ for each mass and scale combination and then locate the extrema of the ratios based on the mass and scale in each case, exactly as in Eqs. (5) and (6) above. Thus the uncertainty band is based on the $R_{p\mathrm{Pb}}$ of each set. Since the ratios are all close to unity (within 20-40% in most cases), and similar to each other, this method would tend to underestimate the uncertainty.

The second, labeled $m/\mu_F/\mu_R\,v2$ on Figs. 18-22, reflects the uncertainty calculation of Eqs. (5) and (6). The maxima and minima of $d\sigma/dX$ are calculated, as in Fig. 17, and then form $R_{p\mathrm{Pb}}$ by dividing by the central value of the $p+p$ cross section in the corresponding rapidity bin (for the p_T-dependent results) or the p_T-integrated cross section (for the rapidity dependence). Thus the shadowing ratios for $v2$ are based on cross sections only. A wider uncertainty band can be expected for this calculation, especially at low p_T.

Note, however, that there is actually no difference between the $v2$ and $v1$ calculations of the uncertainty in the forward-backward ratios because the forward-backward ratios are calculated for each mass and scale combination before calculating the uncertainty to ensure that a one-to-one correspondence is made in R_{FB}. Thus, there is no $v2$ result in the plots of R_{FB}.

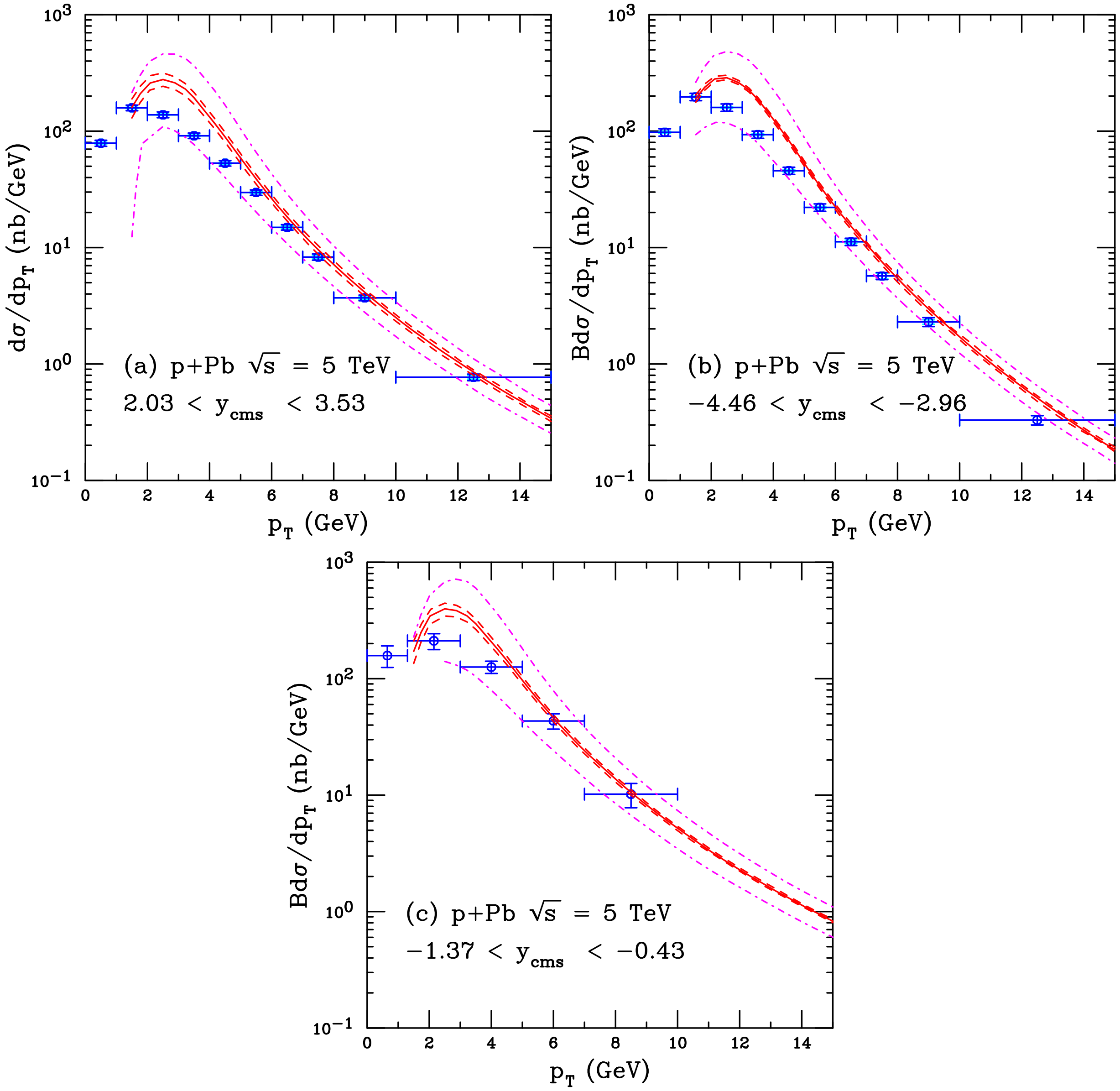

FIG. 17: (Color online) The ALICE J/ψ p_T distributions [2] at forward (a), backward (b) and midrapidity (c) at NLO in the CEM [13]. The solid red curve is the EPS09 NLO central value while the dashed red curves are the EPS09 NLO uncertainties and the dot-dashed magenta curves are the mass and scale uncertainties.

The above methods of calculating the mass and scale uncertainty, relying on Eqs. (5) and (6), are not actually calculated the same way as the EPS09 uncertainty band because they rely only on the extrema of the mass and scale dependent cross sections from the central values rather than adding the excursions from the central value in quadrature, as in the EPS09 uncertainty calculation. Therefore, finally, for $m/\mu_F/\mu_R\, v3$, The mass and scale uncertainties are added in quadrature, a la EPS09, and then form $R_{p\mathrm{Pb}}$ by dividing by the central $p+p$ cross section. Since this is a cumulative uncertainty rather than based on the greatest excursion from the mean, this is expected to give the largest overall uncertainty. The $v3$ uncertainty band was calculated assuming that the appropriate μ_F/m and μ_R/m pairs are $[(H,H),(L,L)]$, $[(H,C),(L,C)]$ and $[(C,H),(C,L)]$. Other choices could lead to different results. (There is only one possible pair for the mass uncertainty thus this part of the calculation is the same for $v2$ and $v3$.)

Results using all three methods are shown for J/ψ and Υ in the remainder of this section.

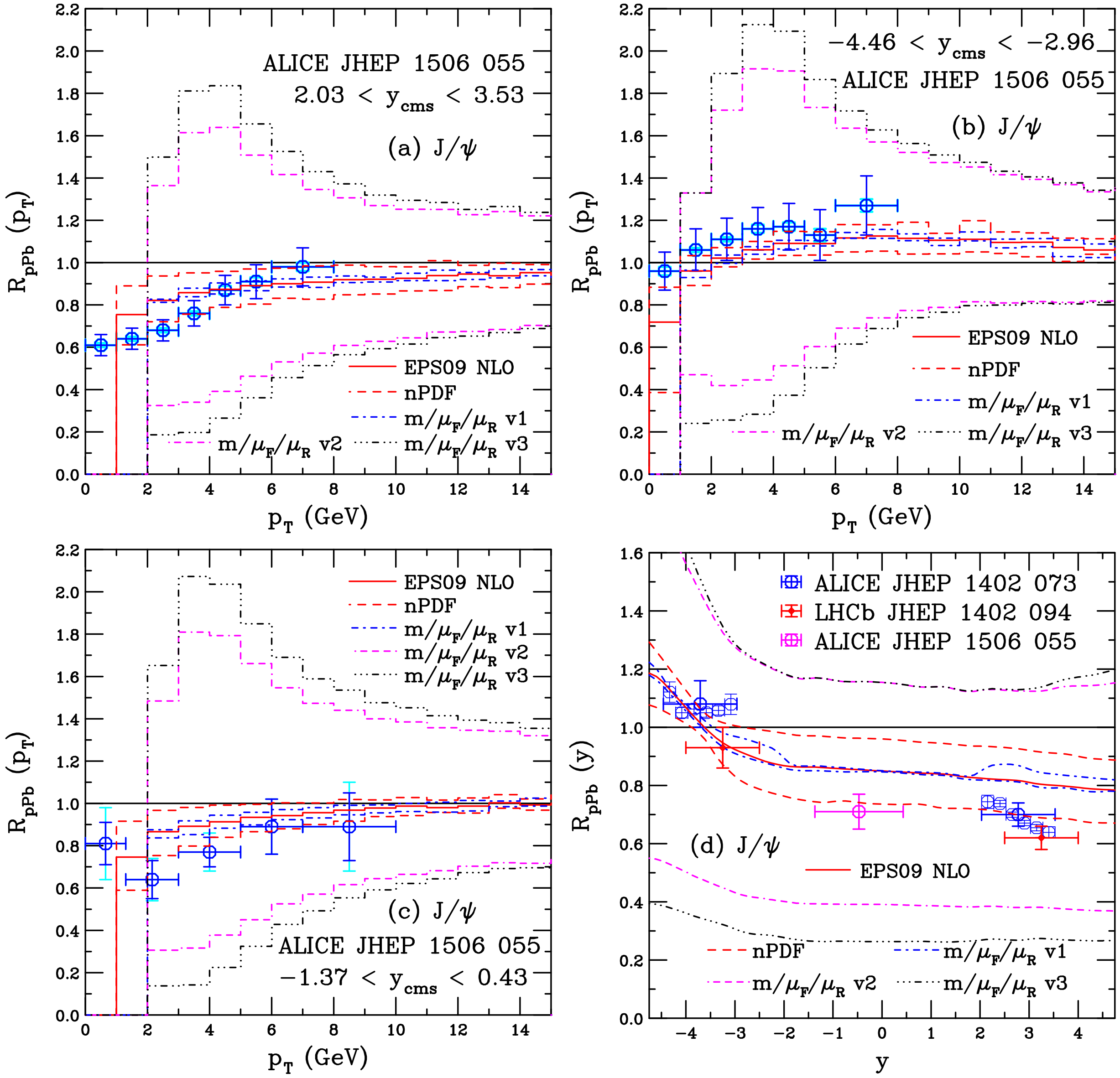

FIG. 18: (Color online) The mass and scale uncertainties in the J/ψ ratio $R_{p\mathrm{Pb}}(p_T)$ in the ALICE acceptance at forward (a), backward (b) and central (c) rapidity [2]. In (d), the ALICE results [1, 2] on $R_{p\mathrm{Pb}}(y)$ are given, $|y| > 0$ in the blue points and midrapidity in magenta, along with those of LHCb [4] (red points). The EPS09 NLO uncertainty band is shown in by the red dashed curves while the uncertainties calculated with method $v1$ are shown in the blue dot-dashed curves; $v2$ in the magenta dot-dash-dash-dashed curves; and $v3$ in the black dot-dot-dot-dashed curves.

1. J/ψ

Figure 18 shows the relative uncertainties for the EPS09 NLO band and the three ways of calculating the mass and scale uncertainty for $R_{p\mathrm{Pb}}$. As expected, the $v1$ proceedure gives the smallest uncertainty since there is little variation in the individual values of $R_{p\mathrm{Pb}}$ for each mass and scale choice for the central EPS09 set. Therefore, the $v1$ band is narrower than that of the EPS09 band itself, underestimating the uncertainty.

On the other hand, the $v2$ and $v3$ bands are wider, especially for $p_T < 5$ GeV, as expected. Also, as mentioned previously, the $v3$ band is broader than that of $v2$ over all p_T although the two methods merge at the highest p_T values. The $R_{p\mathrm{Pb}}(p_T)$ found for the $v2$ method is in agreement with what one might expect looking at the bands on $d\sigma/dp_T$ in Fig. 17. The ratios as a function of p_T are relatively regular even though, at least for $v1$ and $v2$, the combination of factorization and renormalization scales that give the extreme values for that p_T does depend on p_T.

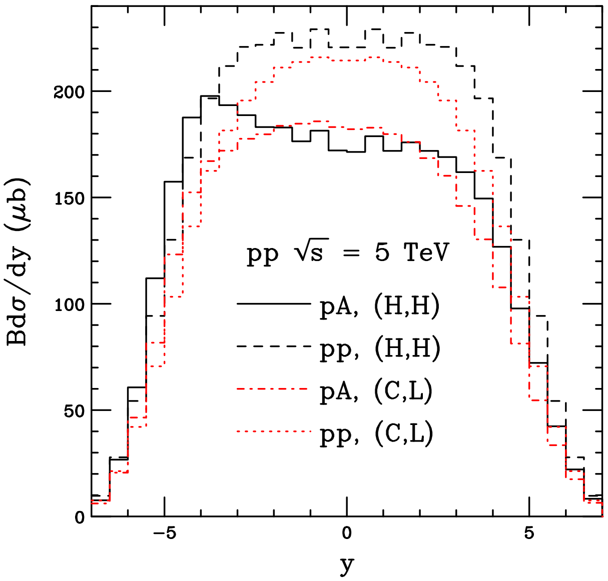

FIG. 19: (Color online) The $p+p$ and p+Pb J/ψ rapidity distributions for the (H,H) (C,L) sets showing the differences leading to the change in the upper limit of the mass and scale uncertainties of method $v1$ around midrapidity. Here the (H,H) results are shown in black (p+Pb solid, $p+p$ dashed) while the (C,L) results are given in red (p+Pb dot-dashed, $p+p$ dotted).

The situation is somewhat different as a function of rapidity, in part because the rapidity distributions fluctuate somewhat, especially at midrapidity. The size of the fluctuations depends on the scale choice and, depending on which scale set determines the extreme value, these fluctuations can manifest themselves in $R_{p\mathrm{Pb}}(y)$. This effect is obvious in Fig. 18(d) where the upper bound on $v1$ is visibly above the central value of the ratio for $|y| > 2$ and almost on top of it for $|y| < 2$. The abrupt change of slope occurs because the maximum value of the ratio is obtained with set (H,H) away from midrapidity and with set (C,L) at midrapidity. This is illustrated in Fig. 19 where the $p+p$ and p+Pb rapidity distributions are shown for each of these combinations. The change in the p+Pb rapidity distribution is a stronger function of y for the (H,H) set than for the (C,L) set. There are also larger fluctuations in the distribution at midrapidity for the (H,H) set. To emphasize this difference, the rapidity distributions are represented as histograms rather than smoothed curves. Note that these fluctuations are not due to limited statistics in the calculation but are more likely due to the uneven distribution of low p_T negative-weight events in the MNR code at midrapidity. The presence of these events may also flatten the rapidity distribution in the LHC energy regime so that while the $p+p$ rapidity distribution is within the mass and scale uncertainty band the slope is somewhat flatter than the measured one, see Ref. [13].

The $v2$ and $v3$ ratios are more separated and, because they are obtained by taking the ratio to the $p+p$ distribution calculated with the central mass and scale set, they are also smoother. The 'kink' in the central EPS09 NLO ratio noted previously is sharpened for the upper limit of these bands and reduced, but still present, in the lower limits. The upper limits obtained for $v2$ and $v3$ are very similar. Indeed these upper limits are almost indistinguishable for most of the illustrated rapidity range. The numerical values are generally different, with the $v3$ values larger than those of $v2$, but the difference is not large enough to be visible on the scale of the plot. This similarity likely stems from the aforementioned fluctuations in the rapidity distributions. Since these fluctuations tend to be smaller for the lower limits of $R_{p\mathrm{Pb}}(y)$, there is a large separation between the lower bounds on $v2$ and $v3$.

In all the cases shown, except for the ratios calculated with $v1$, the envelope of ratios described by the mass and scale uncertainties contains the data. This can be expected because this is the designed purpose of Eqs. (5) and (6) for the $p+p$ distributions and, when applied correctly, it does the same for the nuclear suppression factor $R_{p\mathrm{Pb}}$ as well.

This is not necessarily the case for the forward-backward ratios, shown in Fig. 20. Indeed, in this case the ratios calculated with methods $v1$ and $v3$ are nearly identical. Recall that there is no difference between $v1$ and $v2$ uncertainties for the forward-backward ratios. The most interesting thing to note here is that the ratios of the mass and scale uncertainty as a function of rapidity have different slopes than those of the EPS09 NLO uncertainty. The stronger rise in $R_{p\mathrm{Pb}}(y)$ at backward rapidity, combined with the weak dependence on rapidity in the forward direction makes the upper limit on the mass and scale dependence larger than the central EPS09 set at $y < 2$. At larger rapidities,

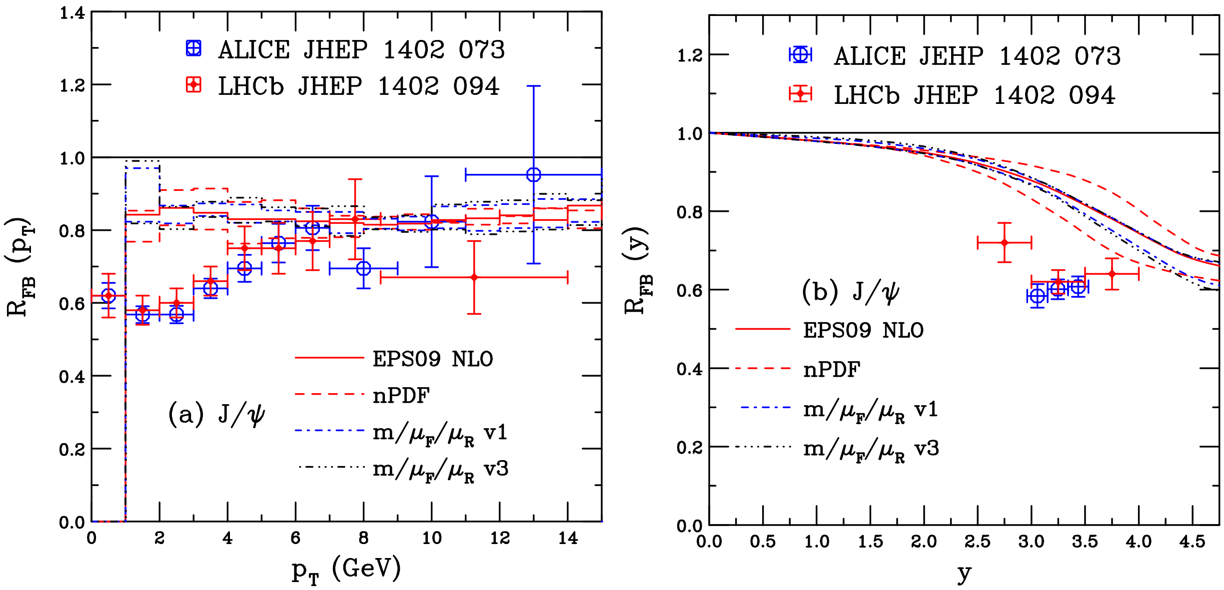

FIG. 20: (Color online) The mass and scale uncertainties in the J/ψ forward-backward ratio $R_{FB}(p_T)$ in the ALICE overlap region (a) and $R_{FB}(y)$ (b). The EPS09 NLO uncertainty band is by the red dashed curves while the uncertainties calculated with method $v1$ are shown in the blue dot-dashed curves and $v3$ in the black dot-dot-dot-dashed curves. The ALICE [1] (blue) and LHCb [4] (red) data are also shown.

these values are almost coincident. On the other hand, the weaker rise in $R_{p\rm Pb}(y)$ for the lower limit in the backward direction makes the lower limit of the forward-backward ratio decrease more rapidly than the central set for $y > 3$.

2. Υ

The results for the mass and scale uncertainties on the ratios for Υ production are presented in Figs. 21 and 22. Overall the trends are quite similar to those for the J/ψ even though the p_T-dependent results here are almost independent of p_T. However, note that the results for $R_{p\rm Pb}$ show much smaller differences between $v2$ and $v3$ over the entire p_T range, as well as a function of rapidity. In this case also, the shape of the limits on the mass and scale uncertainty bands for $R_{p\rm Pb}(y)$ is the same as that of the central EPS09 NLO value so the shape of that ratio has a weaker scale dependence than the J/ψ. The band on $R_{p\rm Pb}(y)$ is broad enough to encompass the range of the low statistics Υ data.

The uncertainties on the forward-backward ratio in Fig. 22 are again small. They are, in fact, considerably smaller than those due to EPS09 which, as seen previously, is not because the uncertainties on the distributions in an individual rapidity bin, for $R_{FB}(p_T)$, are small. Instead, these uncertainties are somewhat canceled in the ratio, even though the largest excursion from the central value can still be expected for $v3$.

F. Factorization

The question of whether cold nuclear matter effects factorize has been much discussed. If so, then at the same energy, the product of the nuclear modification factors at forward and backward rapidity in pA collisions would give the predicted cold matter result for $A + A$ collisions at the same energy.

In their latest paper on the J/ψ p+Pb results [2], the ALICE Collaboration compared the product of their $R_{p\rm Pb}(p_T)$ ratios in the forward and backward rapidity regions at $\sqrt{s_{_{NN}}} = 5.02$ TeV, $2.03 < y_{\rm cms} < 3.53$ and $-4.46 < y_{\rm cms} < -2.96$ respectively, to the $R_{\rm PbPb}(p_T)$ ratio in the region $2.5 < y < 4.0$ (symmetric around midrapidity) at $\sqrt{s_{_{NN}}} = 2.76$ TeV. They did the same for the square of the midrapidity ratio measured in $-1.37 < y_{\rm cms} < -0.43$ in p+Pb collisions at $\sqrt{s_{_{NN}}} = 5.02$ TeV to $R_{\rm PbPb}$ in $|y| < 0.8$ at $\sqrt{s_{_{NN}}} = 2.76$ TeV. From these comparisons they were able to obtain an estimate of the cold nuclear matter effects on Pb+Pb collisions, assuming that the ratios in the forward and backward regions factorize. They then used their p+Pb measurements at the higher energy to form the ratio

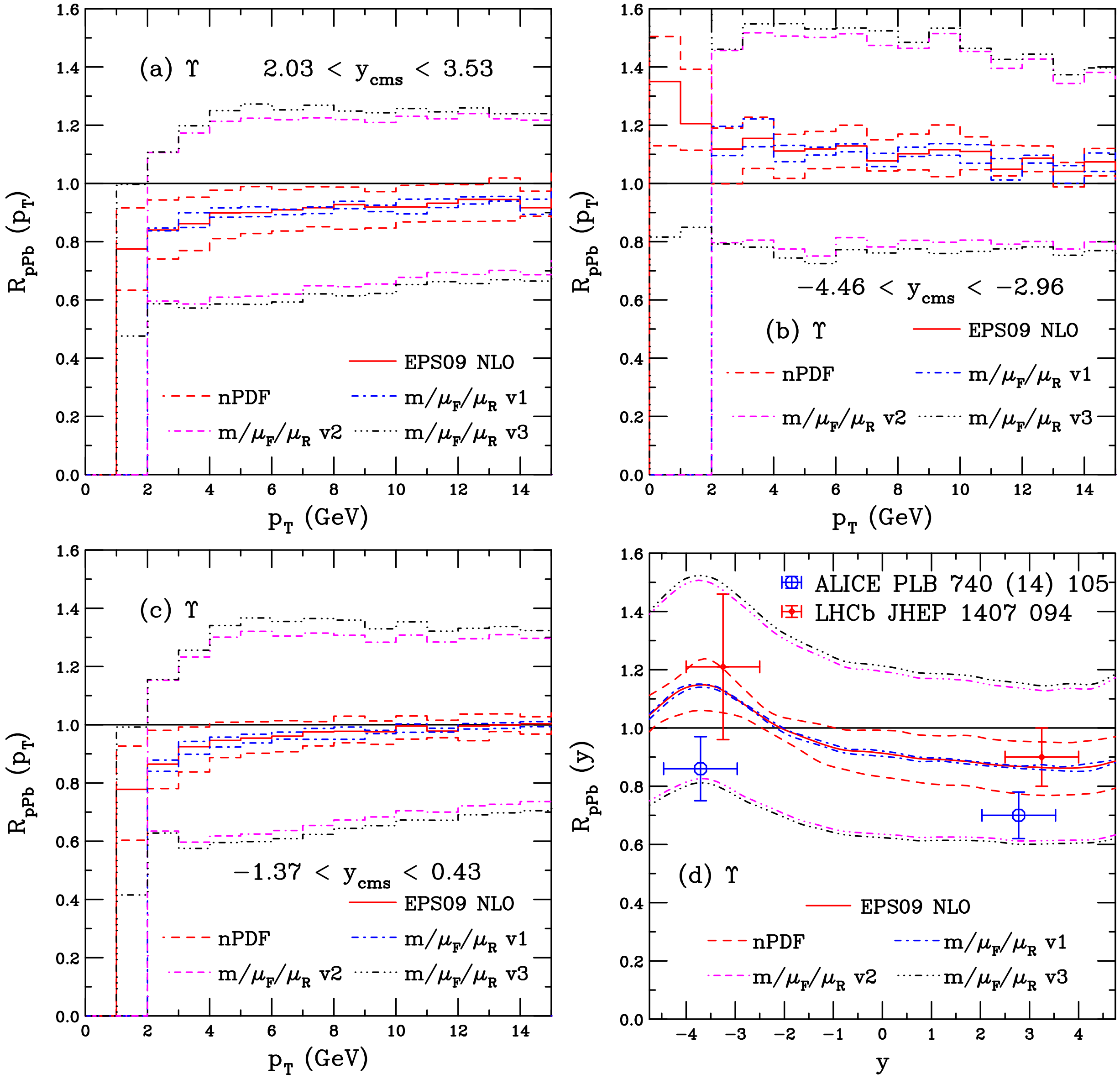

FIG. 21: (Color online) The mass and scale uncertainties in the Υ ratio $R_{p\text{Pb}}(p_T)$ in the ALICE acceptance at forward (a), backward (b) and central (c) rapidity. The ratio $R_{p\text{Pb}}(y)$ is compared to the ALICE [3] (blue) and LHCb [5] (red) data in (d). The EPS09 NLO uncertainty band is shown by the red dashed curves while the uncertainties calculated with method $v1$ are shown in the blue dot-dashed curves; $v2$ in the magenta dot-dash-dash-dashed curves; and $v3$ in the black dot-dot-dot-dashed curves.

$S_{J/\psi} = R_{\text{PbPb}}/(R_{p\text{Pb}}(+y) \times R_{p\text{Pb}}(-y))$. From this comparison, they were able to deduce that, at least for their dimuon measurement, the Pb+Pb data are significantly more surpressed than expected for cold matter effects alone [2].

However, the comparison in Ref. [2] is made for different rapidity regions due to the asymmetric beams in p+Pb collisions. In addition, the difference in the nucleon-nucleon center of mass energy is almost a factor of two. These two effects will cause the x values probed in p+Pb and Pb+Pb collisions to be shifted so that the correspondence is not exact.

In this section, the $R_{p\text{Pb}}$ and R_{PbPb} ratios at LO (rapidity only) and NLO (rapidity and p_T in symmetric forward and backward regions) are compared at the same energy for p+Pb and Pb+Pb so that the correspondence between the x values should be exact. In addition, since the same $\sqrt{s_{_{NN}}}$ is employed, there no rapidity shift in p+Pb relative to Pb+Pb. It is thus possible to check this factorization does indeed explicitly hold for shadowing effects in the CEM.

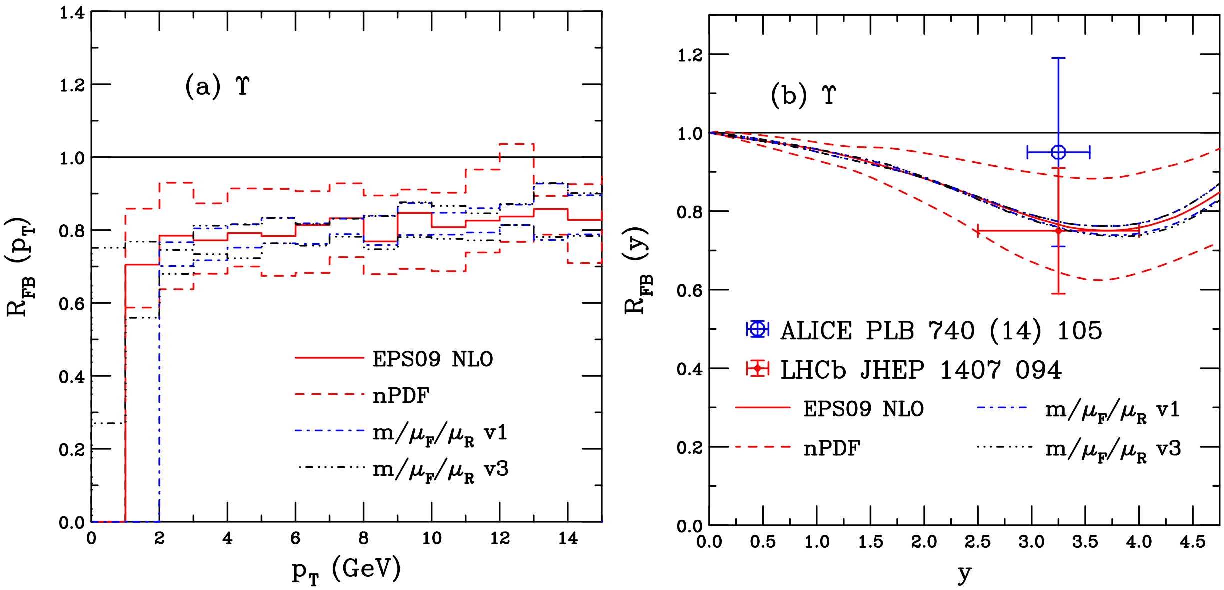

FIG. 22: (Color online) The mass and scale uncertainties in the ϒ forward-backward ratio $R_{FB}(p_T)$ in the ALICE overlap region (a) and $R_{FB}(y)$ (b). The EPS09 NLO uncertainty band is shown by the red dashed curves while the uncertainties calculated with method $v1$ are shown in the blue dot-dashed curves and $v3$ in the black dot-dot-dot-dashed curves. The ALICE [3] (blue) and LHCb [5] (red) data are also shown in (b).

In the calculations here, the central EPS09 sets are employed. The results should be similar for other nPDF sets.

It is straightforward to make this comparison at leading order in the color evaporation model (CEM) where the p_T of the $Q\overline{Q}$ pair is zero and the x_1 and x_2 values are related to the quarkonium rapidity by $x_1, x_2 = (M/\sqrt{s})\exp(\pm y)$. As long as factorization is assumed for the parton densities, the individual shadowing ratios applied to each also factorize. The result is compared for the EPS09 LO central shadowing set in Figs. 23(a) and 24(a) for $\sqrt{s_{NN}} = 2.76$ TeV. In these $2 \to 1$ kinematics, the relation $R_{AA}(y) = R_{pA}(y) \times R_{pA}(-y)$ is exact.

Here the dashed and dot-dashed curves show the ratios $R_{p\mathrm{Pb}}$ at positive and negative rapidities respectively. (In this case, the $-y$ refers to the ion beam moving toward positive rapidity while $+y$ is the standard assumption that the proton beam moves toward positive rapidity, the convention adopted throughout this paper.) The blue dots represent the product of $R_{p\mathrm{Pb}}(+y)$ and $R_{p\mathrm{Pb}}(-y)$. At LO, they lie exactly on top of the red solid curve calculated for Pb+Pb.

A consequence of the lower energy is that the antishadowing peak moves close to midrapidity. This effect is most clearly seen for the ϒ in Fig. 24(a) where the drop into the EMC region and the subsequent rise into the Fermi motion region at high x is clearly visible.

It is also obvious, both for the J/ψ and ϒ, that the Pb+Pb ratio gives stronger shadowing at midrapidity than at forward (and backward) rapidity since, at $y \sim 0$, the ratios $R_{p\mathrm{Pb}}$ at $\pm y$ are both less than unity while, at $2.5 < |y| < 4.0$, these ratios are in the antishadowing region. Therefore, the combination of the two in Pb+Pb interactions is always less than unity with stronger shadowing at midrapidity.

This was also the case for RHIC cold matter $A + A$ calculations at $\sqrt{s_{NN}} = 200$ GeV [23]. More suppression is predicted at $y = 0$ than at forward and backward rapidities with all the shadowing parameterizations for both J/ψ and ϒ production. At RHIC, the $A + A$ data are more suppressed at forward rapidity than at central rapidity, both in the minimum bias data as a function of rapidity and as a function of collision centrality, as quantified by the number of participant nucleons. Standard models of shadowing alone or shadowing with absorption by nucleons in cold nuclear matter or shadowing combined with dissociation in a quark-gluon plasma leads to strong suppression at central rapidities. However, J/ψ regeneration by dynamical coalescence of c and $\overline{c}$ quarks in the medium [39, 61] is biased toward central rapidities and could lead to more suppression at forward rapidity relative to central rapidity since the rapidity distribution of J/ψ production by coalescence is expected to be narrower than the initial J/ψ rapidity distribution [61]. Thus, with coalescence, there should be more suppression at forward y than at midrapidity. Statistical coalescence [62], which is based only on the energy density of the medium, which is higher at $y \sim 0$, would also support this picture.

The same trend has been observed at the LHC, see Ref. [28] and references therein. Coalescence production of the J/ψ should be more important than at RHIC since more $c\overline{c}$ pairs are created in a central Pb+Pb collision at

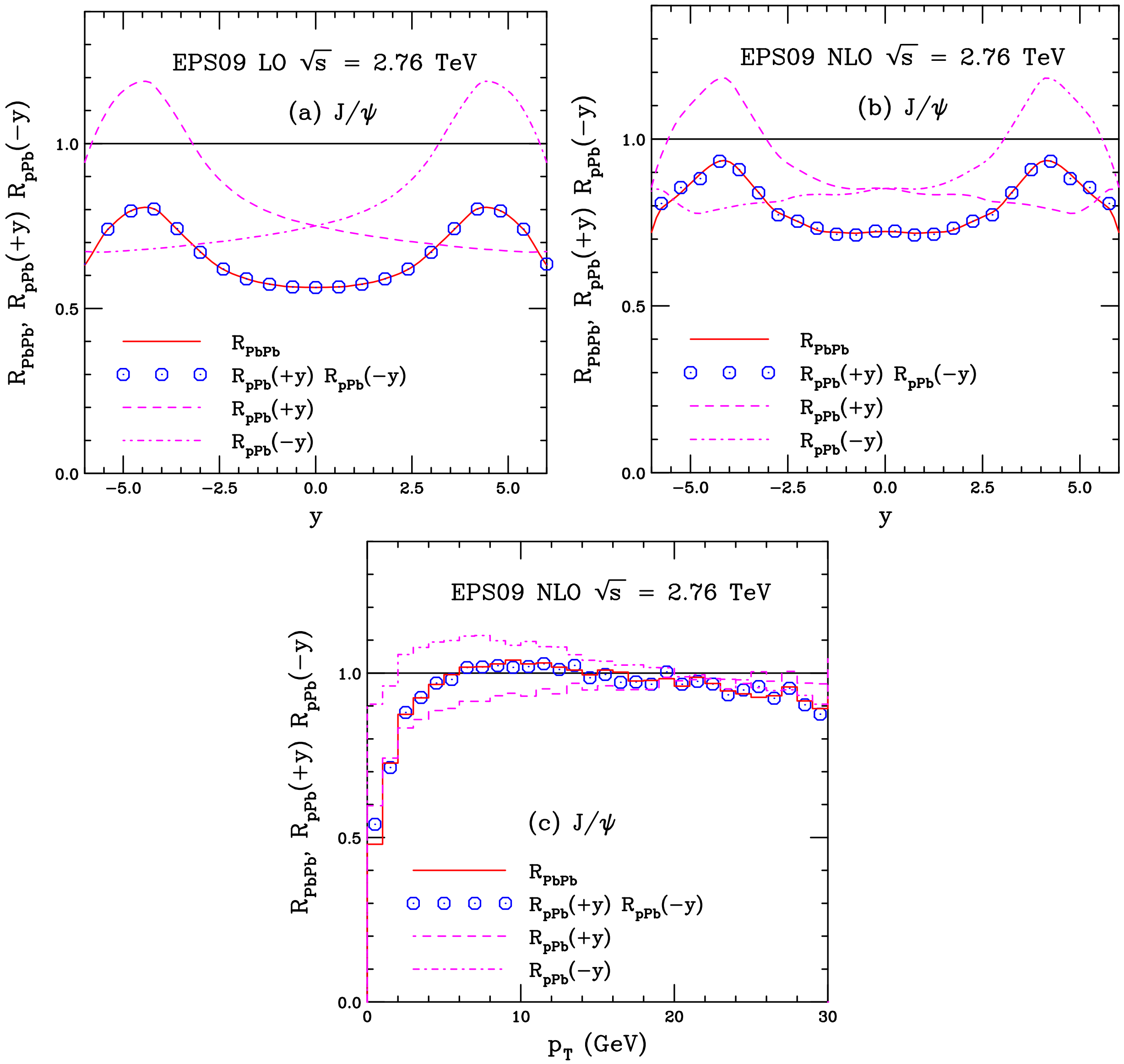

FIG. 23: (Color online) The J/ψ R_{AA} (red solid) ratio is compared to the product $R_{pA}(+y) \times R_{pA}(-y)$ (blue points) along with the individual pA ratios at forward (magenta dashed) and backward (magenta dot-dashed) rapidity. Results are compared for the rapidity distributions at LO (a) and NLO (b) as well as for the p_T dependence at NLO (c). Note that no y direction is given to $R_{\rm PbPb}$ because it is symmetric around $y = 0$.

$\sqrt{s_{NN}} = 2.76$ TeV. Υ production by coalescence at the LHC can be expected to be similar to that expected for the J/ψ at RHIC since the $b\overline{b}$ production cross section at the LHC will be similar to the $c\overline{c}$ production cross section at RHIC [23].

At next-to-leading order, the assumption of factorization of shadowing is less straightforward because quarkonium production in the CEM includes a large contribution from $2 \rightarrow 3$ diagrams so that the correlation between the initial momentum fractions x_1 and x_2 with the rapidity of the quarkonium state is weaker, particularly for high p_T. However, factorization is seen to still hold as a function of rapidity at NLO, as shown in Figs. 23(b) and 24(b), calculated with the EPS09 NLO central set, also at $\sqrt{s_{NN}} = 2.76$ TeV. There are some small fluctuations in the points relative to the curve but these are within the size of the points and are therefore negligible.

Note, however, that there is a significant difference in the shape of the shadowing ratios as a function of rapidity between the LO and NLO results of Figs. 23(a) and (b) as well as between Figs. 24(a) and (b). As discussed in Sec. VI C, this is due to the differences in the EPS09 LO and NLO sets themselves and gives some indication of the

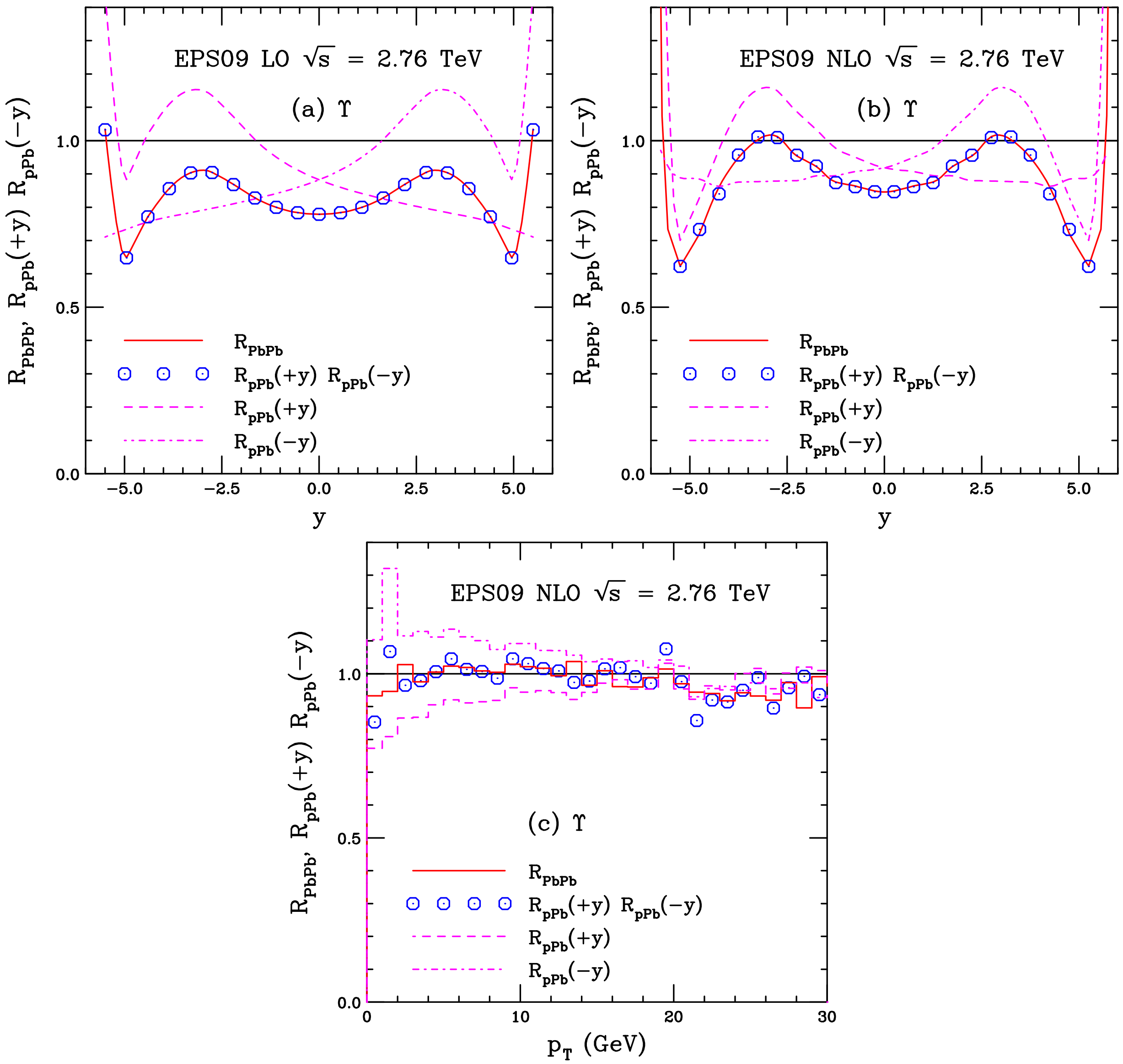

FIG. 24: (Color online) The ϒ R_{AA} (red solid) ratio is compared to the product $R_{pA}(+y) \times R_{pA}(-y)$ (blue points) along with the individual pA ratios at forward (magenta dashed) and backward (magenta dot-dashed) rapidity. Results are compared for the rapidity distributions at LO (a) and NLO (b) as well as for the p_T dependence at NLO (c). Note that no y direction is given to $R_{\rm PbPb}$ because it is symmetric around $y = 0$.

uncertainty inherent in the extraction of the nuclear gluon density.

Finally, the p_T dependence at NLO, unavailable in the CEM at LO, is discussed. One might expect to see the largest deviations in this comparison because of the different kinematics in $2 \to 2$ and $2 \to 3$ interactions in the CEM at NLO. At high p_T, the $2 \to 3$ kinematics is dominant. However, the agreement between the factorized product and the direct Pb+Pb calculation is very good for both J/ψ and ϒ up to quite high p_T, see Figs. 23(c) and 24(c). (The result is shown up to $p_T = 30$ GeV.) There are more fluctuations in the ϒ calculations. Despite this, the agreement is still very good.

The comparisons shown here, at the same energy for both p+Pb and Pb+Pb collisions, demonstrate that the cold matter effects due to shadowing in heavy-ion collisions can be effectively deduced from proton-nucleus collisions, preferably at the same energy.

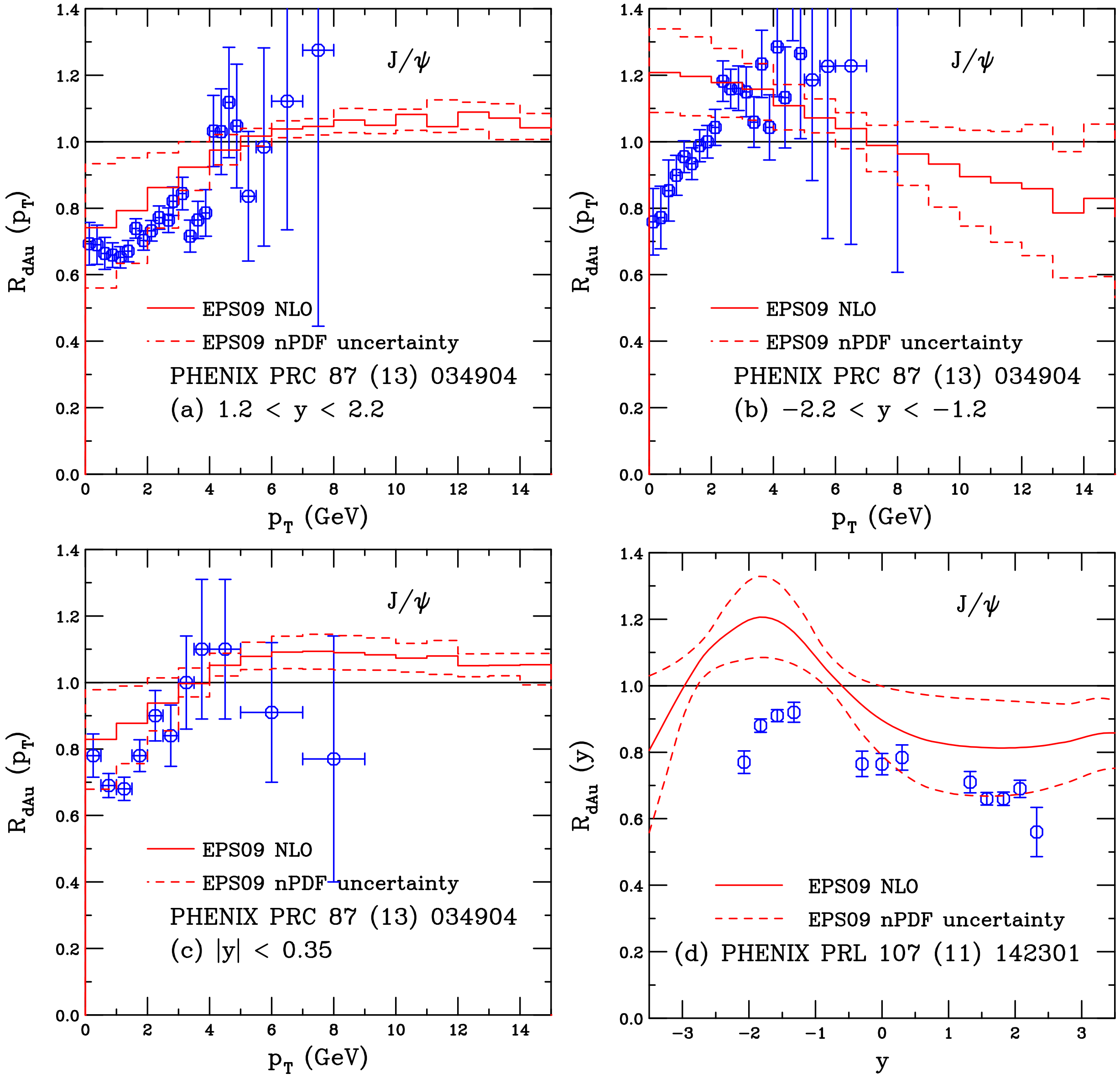

FIG. 25: (Color online) The J/ψ ratio $R_{\rm dAu}(p_T)$ from PHENIX at forward (a), backward (b) and central (c) rapidity [63]. The ratio $R_{\rm dAu}(y)$ [64] is shown (d). The EPS09 NLO uncertainty band is compared to the data.

G. Comparison to RHIC results

Finally, the EPS09 NLO calculations are compared to the RHIC J/ψ and Υ data in Figs. 25 and 26. No absorption is included here, even though the absorption cross section may be non-negiglble at RHIC energies. The EPS09 LO calculations were employed by the PHENIX Collaboration [63] to extract the putative absorption cross section required to make a shadowing and absorption scenario agree with the data. The NLO calculations are presented as a function of p_T and rapidity together for the first time.

The J/ψ p_T-dependent data, shown in Fig. 25(a)-(c), follows approximately the same trend at forward, backward and midrapidity. At $p_T \sim 0$, $R_{\rm dAu} \sim 0.7 - 0.8$. The ratio then increases with p_T until becoming compatible with unity, albeit it with rather poor statistics, at $p_T \geq 4$ GeV. At forward and midrapidity the calculations agree with the trends of the data rather well. At low p_T, the x range is in the shadowing region but moves toward the antishadowing region as p_T increases, see the shape of $R_{\rm dAu}(y)$ in Fig. 25(d). However, at backward rapidity at RHIC, the calculations suggest that, at low p_T, the antishadowing region is probed while, at higher p_T, the EMC region is reached. Thus,

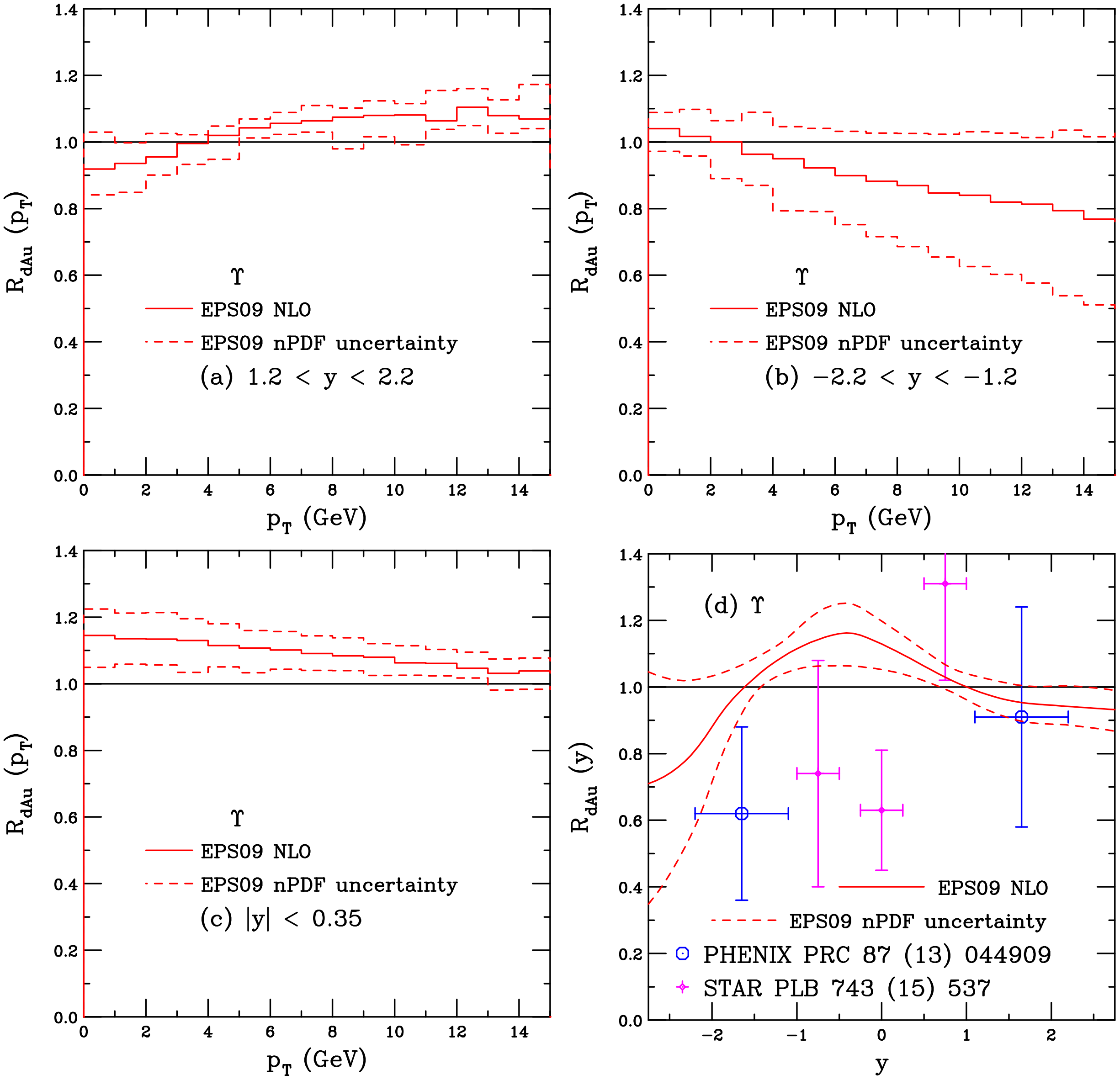

FIG. 26: (Color online) The Υ ratio $R_{\rm dAu}(p_T)$ for RHIC at forward (a), backward (b) and central (c) rapidity. The ratio $R_{\rm dAu}(y)$ is also shown (d). The EPS09 NLO uncertainty band is compared to the PHENIX [65] (blue circles) and STAR [66] (magenta crosses) $R_{\rm dAu}(y)$ data in (d).

for $p_T < 2$ GeV, the trend of the data and the calculations are opposite. For $p_T > 2$ GeV, the uncertainties in the data and the calculations are large enough for the results to be compatible.

A recent calculation studied the centrality dependence of gluon shadowing. The impact parameter dependence, together with a rapidity-dependent absorption cross section, was extracted from the centrality dependence of $R_{\rm dAu}(y)$ [6]. The large absorption cross section required at backward rapidity was explained in the context of an expanding color octet that reaches its final-state size at backward rapidity but has a negligible effect at forward rapidity because the primordial J/ψ passes through the target before reaching its full size [55]. Presumably, this would also have the desired effect on the p_T dependence in the backward region since low p_T J/ψ's will be strongly absorbed in this region while those at higher p_T will again pass through the transverse direction of the target before fully forming, maintaining the agreement of the calculation with the data at higher p_T.

Finally, the Υ results shown in Fig. 26 are discussed. There is only limited data for the Υ, including the low statistics PHENIX [65] and STAR [66] data presented in Fig. 26(d). The uncertainties on the measurements, along with the large uncertainties in the calculation at backward rapidity, allow the calculation and the data to agree within the errors, except for the STAR point at $y \sim 0$. Although it has the lowest statistical uncertainty, it exhibits strong suppression in a rapidity region where antishadowing is predicted. The p_T dependence has not yet been measured.

The calculated p_T dependence in the forward region, Fig. 26(a), is already entering the antishadowing region for $p_T > 6$ GeV. At midrapidity, the entire p_T range is in this region so that $R_{\rm dAu}(p_T) > 1$ for all p_T. On the other hand, at backward rapidity, most of the p_T region is, in fact, in the EMC region where the uncertainies in the calculated $R_{\rm dAu}(p_T)$ are large, see Fig. 26(b).

It is unlikely that the situation for Υ can be improved with the current RHIC detectors. However, the future sPHENIX detector [67] is expected to be able to separate the three Υ(S) states. This improved mass resolution, together with the higher efficiency expected for sPHENIX and higher luminosity of the sPHENIX runs, means that the p_T dependence could be measured, if a d+Au run is made during the sPHENIX lifetime.

VII. SUMMARY

The results with EPS09 NLO shadowing agree with the measured $R_{p\rm Pb}$ within the uncertainties of both the calculation and the data. However, the forward-backward ratios, independent of the interpolated $p+p$ baseline, are not as well described by EPS09 NLO. Any general conclusion about this apparent discrepancy awaits $p+p$ data at the same energy to check the interpolation schemes employed. The older EKS98 LO parameterization, although not applied consistently in a NLO calculation, does the best job of describing all the data.

The shadowing parameterizations used in this study exhibit a wide range of behavior for the nuclear gluon density at low x, an x region outside the current range of the fits from fixed-target nDIS data at higher x and low μ^2. If nuclear data were available from high energy $e+A$ collisions, the nuclear gluon densities could be more precisely pinned down by global analyses of the scale dependence of the nuclear structure functions. In hadroproduction, direct photon or open charm production, dominated by gluon-induced processes but without the additional complexities of nuclear absorption, could be utilized to study the nuclear gluon density. The LHC data, with the lower x reach, should be incorporated into a new fit of the nuclear parton densities.

Of the cold matter effects not included in this work, neither absorption by nucleons or dissociation by comovers is expected to have a strong effect on the shape of $R_{p\rm Pb}$. These effects, especially comover dissociation, would have a greater impact on the suppression factor for the excited states, as discussed in Ref. [57]. Absorption of a fully formed quarkonium state is only possible at large negative rapidities at the LHC and thus does not have a significant impact on the ground state (J/ψ and $\Upsilon(1S)$) suppression factors [54]. The formation time argument also limits the impact of absorption on the excited quarkonium states [55]. The largest effect on the shape of $R_{p\rm Pb}$, other than shadowing, which might improve the agreement with the data, is energy loss in cold matter. However, the magnitude of the energy loss parameter depends on the shadowing parameterization used in conjunction with it [10, 52, 53]. Thus, perhaps, global analyses of the nuclear parton densities should allow for other initial-state effects to be included or the subject of final-state energy loss returned to after a new global analysis of the nuclear parton densities has been performed.

In conclusion note that, since absorption is assumed to be negligible at the LHC and include no other cold nuclear matter effects, the uncertainties on the ratios can be obtained from the EPS09 NLO bands shown in the figures. However, if other effects are incorporated, a more extensive error analysis, including the uncertainties on these additional effects, would be necessary.

Acknowledgements

The numerical values of the ratios shown in this paper are available from the author. I thank R. Arnaldi, W. Brooks, K. J. Eskola, and E. Scomparin for discussions.

This work was performed under the auspices of the U.S. Department of Energy by Lawrence Livermore National Laboratory under Contract DE-AC52-07NA27344. The author would also like to acknowledge the Institute for Nuclear Theory at the University of Washington in Seattle for the hospitality at the beginning of this work.

---

[1] B. Abelev *et al.* (ALICE Collaboration), J/ψ production and nuclear effects in p+Pb collisions at $\sqrt{s_{_{NN}}} = 5.02$ TeV, JHEP **1402**, 073 (2014).

[2] J. Adam *et al.* (ALICE Collaboration), Rapidity and transverse-momentum dependence of the inclusive J/ψ nuclear modification factor in p+Pb collisions at $\sqrt{s_{_{NN}}} = 5.02$ TeV, JHEP **1506**, 055 (2015).

[3] B. B. Abelev *et al.* (ALICE Collaboration), Production of inclusive Υ(1S) and Υ(2S) in p+Pb collisions at $\sqrt{s_{_{NN}}} = 5.02$ TeV, Phys. Lett. B **740**, 105 (2014).

[4] R. Aaij *et al.* (LHCb Collaboration), Study of J/ψ production and cold nuclear matter effects in p+Pb collisions at $\sqrt{s_{_{NN}}} = 5$ TeV, JHEP **1402**, 072 (2014).

[5] R. Aaij *et al.* (LHCb Collaboration), Study of Υ production and cold nuclear matter effects in p+Pb collisions at $\sqrt{s_{_{NN}}} = 5$ TeV, JHEP **1407**, 094 (2014).

[6] D. C. McGlinchey, A. D. Frawley and R. Vogt, Impact parameter dependence of the nuclear modification of J/ψ production in d+Au collisions at $\sqrt{s_{_{NN}}} = 200$ GeV, Phys. Rev. C **87**, 054910 (2013).

[7] A. D. Frawley and R. Vogt, in progress.

[8] R. Vogt, Cold Nuclear Matter Effects on J/ψ and Υ Production at the LHC, Phys. Rev. C **81**, 044903 (2010).

[9] J. L. Albacete *et al.*, Predictions for p+Pb Collisions at $\sqrt{s_{_{NN}}} = 5$ TeV, Int. J. Mod. Phys. E **22**, 1330007 (2013).

[10] R. Vogt, Predictions for p+Pb collisions at $\sqrt{s_{_{NN}}} = 5$ TeV: expectations vs. data, Nucl. Phys. A **932**, 494 (2014).

[11] R. Vogt (JET Collaboration), Predictions for p+Pb collisions at $\sqrt{s_{_{NN}}} = 5$ TeV: expectations vs. data, Nucl. Phys. A **931**, 371 (2014).

[12] R. Vogt, J/ψ's are jazzy, Nucl. Phys. A **928**, 222 (2014).

[13] R. E. Nelson, R. Vogt and A. D. Frawley, Narrowing the uncertainty on the total charm cross section and its effect on the J/ψ cross section, Phys. Rev. C **87** (2013) 014908.

[14] R. E. Nelson, R. Vogt and A. D. Frawley, in preparation.

[15] B. B. Abelev *et al.* (ALICE Collaboration), Suppression of ψ(2S) production in p+Pb collisions at $\sqrt{s_{_{NN}}} = 5.02$ TeV, JHEP **1412**, 073 (2014).

[16] G. Aad *et al.* (ATLAS Collaboration), Measurement of differential J/ψ production cross sections and forward-backward ratio in p+Pb collisions with the ATLAS detector, arXiv:1505.08141 [hep-ex].

[17] N. Filipovic (CMS Collaboration), Quarkonia in $p + p$, p+Pb, and Pb+Pb collisions with CMS, presented at Hard Probes 2015, https://indico.triumf.ca/sessionDisplay.py?sessionId=38&slotId=0&confId=1922#2015-06-30; http://CMSPublic/PhysicsResultsHIN14009 (2015).

[18] S. Chatrchyan *et al.* (CMS Collaboration), Event activity dependence of $\Upsilon(n$S) production in $\sqrt{s_{_{NN}}} = 5.02$ TeV p+Pb and $\sqrt{s} = 2.76$ TeV $p + p$ collisions, JHEP **1404**, 103 (2014).

[19] R. Gavai, D. Kharzeev, H. Satz, G. A. Schuler, K. Sridhar and R. Vogt, Quarkonium production in hadronic collisions, Int. J. Mod. Phys. A **10**, 3043 (1995) [arXiv:hep-ph/9502270].

[20] J. F. Amundson, O. J. P. Eboli, E. M. Gregores and F. Halzen, Quantitative tests of color evaporation: Charmonium production, Phys. Lett. B **390**, 323 (1997).

[21] G. A. Schuler and R. Vogt, Systematics of quarkonium production, Phys. Lett. B **387**, 181 (1996).

[22] M. L. Mangano, P. Nason, and G. Ridolfi, Heavy quark correlations in hadron collisions at next-to-leading order, Nucl. Phys. B **373**, 295 (1992).

[23] A. D. Frawley, T. Ullrich and R. Vogt, eavy flavor in heavy-ion collisions at RHIC and RHIC II, Phys. Rept. **462**, 125 (2008).

[24] M. L. Mangano, P. Nason, and G. Ridolfi, Fixed target hadroproduction of heavy quarks, Nucl. Phys. B **405**, 507 (1993).

[25] M. Cacciari, P. Nason and R. Vogt, QCD predictions for charm and bottom production at RHIC, Phys. Rev. Lett. **95**, 122001 (2005).

[26] Y. Q. Ma, J. W. Qiu, G. Sterman and H. Zhang, Factorized power expansion for high-p_T heavy quarkonium production, Phys. Rev. Lett. **113**, no. 14, 142002 (2014)

[27] R. Maciula and A. Szczurek, Open charm production at the LHC - k_t-factorization approach, Phys. Rev. D **87**, 094022 (2013).

[28] N. Brambilla *et al.*, QCD and Strongly Coupled Gauge Theories: Challenges and Perspectives, Eur. Phys. J. C **74**, 2981 (2014).

[29] Y. Feng, J. P. Lansberg and J. X. Wang, Energy Dependence of Direct-Quarkonium Production in $p + p$ Collisions from Fixed-Target to LHC Energies: Complete One-Loop Analysis, arXiv:1504.00317 [hep-ph].

[30] Y. Q. Ma and R. Venugopalan, Comprehensive Description of J/ψ Production in Proton-Proton Collisions at Collider Energies, Phys. Rev. Lett. **113**, 192301 (2014).

[31] Y. Q. Ma, R. Venugopalan and H. F. Zhang, J/ψ production and suppression in high energy proton-nucleus collisions, arXiv:1503.07772 [hep-ph].

[32] K. T. Chao, Y. Q. Ma, H. S. Shao, K. Wang and Y. J. Zhang, J/ψ Polarization at Hadron Colliders in Nonrelativistic QCD, Phys. Rev. Lett. **108**, 242004 (2012).

[33] P. Faccioli, V. Knnz, C. Lourenco, J. Seixas and H. K. Whri, Quarkonium production in the LHC era: a polarized perspective, Phys. Lett. B **736**, 98 (2014).

[34] H. L. Lai, M. Guzzi, J. Huston, Z. Li, P. Nadolsky, J. Pumplin, C.-P. Yuan, New parton distributions for collider physics, Phys. Rev. D **82**, 074024 (2010).

[35] H. L. Lai *et al.* (CTEQ Collaboration), Global QCD analysis of parton structure of the nucleon: CTEQ5 parton distributions, Eur. Phys. J. C **12**, 375 (2000).

[36] J. Pumplin, D. R. Stump, J. Huston, H. L. Lai, P. M. Nadolsky and W. K. Tung, New generation of parton distributions with uncertainties from global QCD analysis, JHEP **0207**, 012 (2002).

[37] A. D. Martin, W. J. Stirling, R. S. Thorne and G. Watt, Parton distributions for the LHC, Eur. Phys. J. C **63**, 189 (2009).

[38] K. J. Eskola, H. Paukkunen and C. A. Salgado, EPS09: A New Generation of NLO and LO Nuclear Parton Distribution

Functions, JHEP **0904**, 065 (2009).

[39] M. Bedjidian *et al.*, Hard probes in heavy ion collisions at the LHC: Heavy flavor physics, CERN-2004-009-C, arXiv:hep-ph/0311048.

[40] L. Frankfurt, V. Guzey and M. Strikman, Leading Twist Nuclear Shadowing Phenomena in Hard Processes with Nuclei, Phys. Rept. **512**, 255 (2012).

[41] H. L. Lai, J. Huston, S. Kuhlmann, F. Olness, J. Owens, D. Soper, W. K. Tung and H. Weerts, Improved Parton Distributions from Global Analysis of Recent Deep Inelastic Scattering and Inclusive Jet Data, Phys. Rev. D **55**, 1280 (1997).

[42] M. Gluck, E. Reya and A. Vogt, Parton distributions for high-energy collisions, Z. Phys. C **53**, 127 (1992).

[43] K. J. Eskola, V. J. Kolhinen and P. V. Ruuskanen, Scale evolution of nuclear parton distributions, Nucl. Phys. B **535**, 351 (1998).

[44] K. J. Eskola, V. J. Kolhinen and C. A. Salgado, The scale dependent nuclear effects in parton distributions for practical applications, Eur. Phys. J. C **9**, 61 (1999).

[45] M. Gluck, E. Reya and A. Vogt, Dynamical Parton Distributions Revisited, Eur. Phys. J. C **5**, 461 (1998).

[46] D. de Florian and R. Sassot, Nuclear parton distributions at next-to-leading order, Phys. Rev. D **69**, 074028 (2004).

[47] M. J. Leitch *et al.* (E866 Collaboration), Measurement of J/ψ and ψ' suppression in $p + A$ collisions at 800 GeV/c, Phys. Rev. Lett. **84**, 3256 (2000).

[48] I. Abt *et al.* (HERA-B Collaboration), Kinematic distributions and nuclear effects of J/ψ production in 920 GeV fixed-target proton-nucleus collisions, Eur. Phys. J. C **60**, 525 (2009).

[49] R. Vogt, The x_F dependence of ψ and Drell-Yan production, Phys. Rev. C **61**, 035203 (2000).

[50] P. L. McGaughey, Recent measurements of quarkonia and Drell-Yan production in proton nucleus collisions, Nucl. Phys. A **610**, 394c (1996).

[51] N. Brambilla *et al.*, Heavy quarkonium: progress, puzzles, and opportunities, Eur. Phys. J. C **71**, 1534 (2011).

[52] F. Arleo and S. Peigné, Heavy quarkonium suppression in $p + A$ collisions from parton energy loss in cold QCD matter, JHEP **1303** (2013) 122.

[53] F. Arleo, R. Kolevatov, S. Peigné and M. Rustamova, Centrality and p_T dependence of J/ψ suppression in proton-nucleus collisions from parton energy loss, JHEP **1305** (2013) 155.

[54] C. Lourenço, R. Vogt and H. Wöhri, Energy dependence of J/ψ absorption in proton-nucleus collisions, JHEP **0902**, 014 (2009).

[55] F. Arleo, P. B. Gossiaux, T. Gousset and J. Aichelin, Charmonium suppression in $p+A$ collisions, Phys. Rev. C **61**, 054906 (2000).

[56] A. Adare *et al.* [PHENIX Collaboration], Nuclear Modification of ψ', χ_c, and J/ψ Production in d+Au Collisions at $\sqrt{s_{NN}} = 200$GeV, Phys. Rev. Lett. **111**, 202301 (2013).

[57] E. G. Ferreiro, ψ(2S) versus J/ψ suppression in the comover interaction approach, arXiv:1411.0549 [hep-ph].

[58] A. Accardi *et al.*, Electron Ion Collider: The Next QCD Frontier - Understanding the glue that binds us all, arXiv:1212.1701 [nucl-ex].

[59] R. Vogt, Open and hidden charm production at RHIC and LHC, J. Phys. G **31**, S773 (2005).

[60] E. G. Ferreiro, F. Fleuret, J. P. Lansberg and A. Rakotozafindrabe, Impact of the Nuclear Modification of the Gluon Densities on J/ψ production in p+Pb collisions at $\sqrt{s_{NN}} = 5$ TeV, Phys. Rev. C **88** (2013) 047901.

[61] R. L. Thews and M. L. Mangano, Momentum spectra of charmonium produced in a quark-gluon plasma, Phys. Rev. C **73**, 014904 (2006).

[62] A. Andronic, P. Braun-Munzinger, K. Redlich and J. Stachel, Statistical hadronization of charm in heavy ion collisions at SPS, RHIC and LHC, Phys. Lett. B **571**, 36 (2003).

[63] A. Adare *et al.* (PHENIX Collaboration), Transverse-Momentum Dependence of the J/ψ Nuclear Modification in d+Au Collisions at $\sqrt{s_{NN}} = 200$ GeV, Phys. Rev. C **87**, 034904 (2013).

[64] A. Adare *et al.* (PHENIX Collaboration), Cold Nuclear Matter Effects on J/ψ Yields as a Function of Rapidity and Nuclear Geometry in Deuteron-Gold Collisions at $\sqrt{s_{NN}} = 200$ GeV, Phys. Rev. Lett. **107**, 142301 (2011).

[65] A. Adare *et al.* (PHENIX Collaboration), Υ(1S+2S+3S) production in d+Au and $p + p$ collisions at $\sqrt{s_{NN}} = 200$ GeV and cold-nuclear matter effects, Phys. Rev. C **87**, 044909 (2013).

[66] L. Adamczyk *et al.* (STAR Collaboration), Suppression of Υ production in d+Au and Au+Au collisions at $\sqrt{s_{NN}} = 200$ GeV, Phys. Lett. B **735**, 127 (2014) [Phys. Lett. B **743**, 537 (2015)].

[67] A. Adare *et al.* (PHENIX Collaboration), An Upgrade Proposal from the PHENIX Collaboration, arXiv:1501.06197 [nucl-ex].